Disk Life Meter
Annual Report 2004

Dave Mourer, Brian Hazel, and Deb Whitis
General Electric Aircraft Engines, Cincinnati, Ohio

The NASA STI Program Office . . . in Profile

Since its founding, NASA has been dedicated to the advancement of aeronautics and space science. The NASA Scientific and Technical Information (STI) Program Office plays a key part in helping NASA maintain this important role.

The NASA STI Program Office is operated by Langley Research Center, the Lead Center for NASA's scientific and technical information. The NASA STI Program Office provides access to the NASA STI Database, the largest collection of aeronautical and space science STI in the world. The Program Office is also NASA's institutional mechanism for disseminating the results of its research and development activities. These results are published by NASA in the NASA STI Report Series, which includes the following report types:

- TECHNICAL PUBLICATION. Reports of completed research or a major significant phase of research that present the results of NASA programs and include extensive data or theoretical analysis. Includes compilations of significant scientific and technical data and information deemed to be of continuing reference value. NASA's counterpart of peer-reviewed formal professional papers but has less stringent limitations on manuscript length and extent of graphic presentations.

- TECHNICAL MEMORANDUM. Scientific and technical findings that are preliminary or of specialized interest, e.g., quick release reports, working papers, and bibliographies that contain minimal annotation. Does not contain extensive analysis.

- CONTRACTOR REPORT. Scientific and technical findings by NASA-sponsored contractors and grantees.

- CONFERENCE PUBLICATION. Collected papers from scientific and technical conferences, symposia, seminars, or other meetings sponsored or cosponsored by NASA.

- SPECIAL PUBLICATION. Scientific, technical, or historical information from NASA programs, projects, and missions, often concerned with subjects having substantial public interest.

- TECHNICAL TRANSLATION. English-language translations of foreign scientific and technical material pertinent to NASA's mission.

Specialized services that complement the STI Program Office's diverse offerings include creating custom thesauri, building customized databases, organizing and publishing research results . . . even providing videos.

For more information about the NASA STI Program Office, see the following:

- Access the NASA STI Program Home Page at *http://www.sti.nasa.gov*

- E-mail your question via the Internet to help@sti.nasa.gov

- Fax your question to the NASA Access Help Desk at 301–621–0134

- Telephone the NASA Access Help Desk at 301–621–0390

- Write to:
  NASA Access Help Desk
  NASA Center for AeroSpace Information
  7121 Standard Drive
  Hanover, MD 21076

Disk Life Meter
Annual Report 2004

Dave Mourer, Brian Hazel, and Deb Whitis
General Electric Aircraft Engines, Cincinnati, Ohio

National Aeronautics and
Space Administration

Glenn Research Center

Task Order #23
Annual Technical Narrative Progress Report
Disk Life Meter Executive Summary

Objectives

NASA seeks to develop technologies that will enable commercial gas turbine engines to produce fewer emissions and less noise while increasing reliability.

Technologies sought lie in the categories of:
- Turbine Engine Prognostics
- Active Controls for Emissions and Noise reduction
- Active Structural Control
- Modeling, Analysis and System Studies

Work Element 1.1 Disk Life Meter Specific Objectives

Develop materials models and sensors to measure remaining life in turbine disk materials operated at sustained high temperatures of 1200 – 1500 F for up to 20,000 hours.

Initial physical models have been developed and future work can now expand the models and initiate sensor development and system integration towards a "disk life meter" based on remaining disk life using specific part operating conditions.

Subtask 1.1.1 – Alloy Phase Stability (Diffusion Multiples)

In this task, the team developed the advanced analytical techniques to characterize local chemistry effects on precipitation kinetics and morphological stability of gamma-prime during long-time exposure. This technique also has great promise in identifying local deformation mechanisms to calibrate physical model development. GEAE supplied the specimens and background information to enable development of detailed quantitative characterization techniques.

Subtask 1.1.2 - Superalloy Damage and Failure Mechanisms

In this task, the team applied advanced analytical techniques to characterize damage accumulation and failure modes associated with creep deformation, tensile rupture, and hot corrosion. R104 creep deformation modes were shown to be dependent on the stress/temperature regime and novel creep deformation modes were identified. Hot corrosion studies identified detailed aspects of the mechanism and point towards potential techniques to combat field corrosion. Quench crack studies have identified physical and mechanical behavior regimes associated with high and low ductility. Initial microstructural level FEM models have been established to further explore quench behavior. GEAE supplied the specimens and background information to enable detailed quantitative characterization and behavior model development in all three areas.

Contents

List of Figures

List of Tables

1. Technical Progress
1.1 Overview

Initial physical models have been developed and future work can now expand the models and initiate sensor development and system integration towards a "disk life meter" based on remaining disk life using specific part operating conditions.

1.2 Subtask 1.1 – Alloy Phase Stability (Diffusion Multiples)

GEAE provided OSU an initial two samples of diffusion multiples from the DARPA AIM program containing various nickel-based superalloys and pure elements of interest to OSU for advanced micro structural characterization techniques.
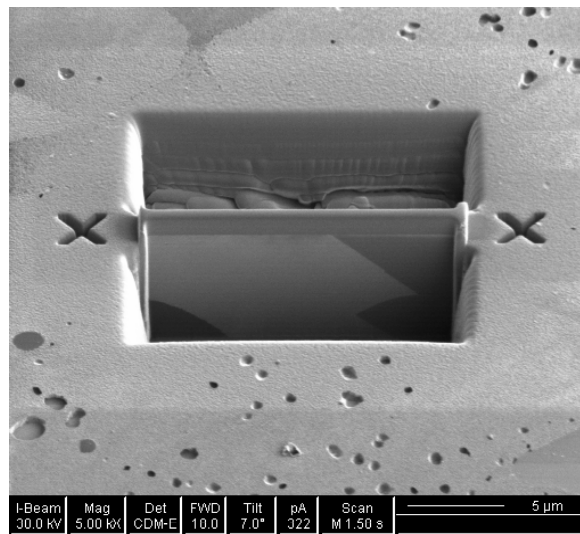
Figure 1 Initial stage of FIB extraction of a foil for EFTEM .

In coordination with GEAE, OSU has established automated FIB routines used to cut and thin membranes at specific distances from the diffusion multiple interfaces. These routines were successful in creating membranes, however, the initial membranes were too thick to be transparent in the transmission electron microscope, even after several technique enhancements/modifications.

The difficulties were overcome by continued refinement of the milling procedure at OSU. To establish the validity of modified thinning techniques, a bulk sample of Rene 104 that was sectioned from the grip end of a creep test specimen. The current techniques were used to prepare a TEM membrane to confirm it was sufficiently thin to perform further characterization work using EFTEM imaging.
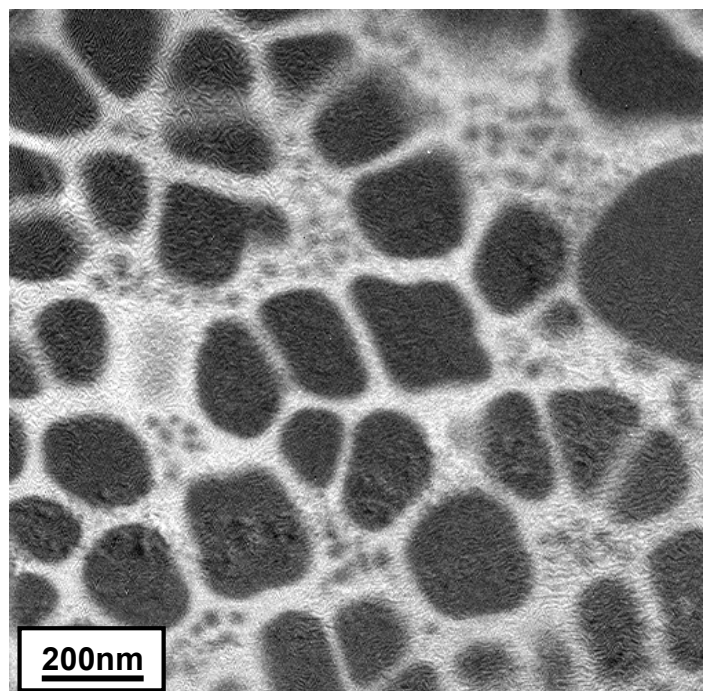
Figure 2 EFTEM image demonstrating high resolution of γ' precipitate morphology including tertiary or aging γ'.

Microstructural characterization of the membranes was conducted using EFTEM imaging and as shown in the accompanying figure excellent resolution was obtained, thus validating the technique.

Chemical Profiling Using Energy Dispersive X-Ray Spectroscopy

Example: EDX line profile of a nickel-based superalloy
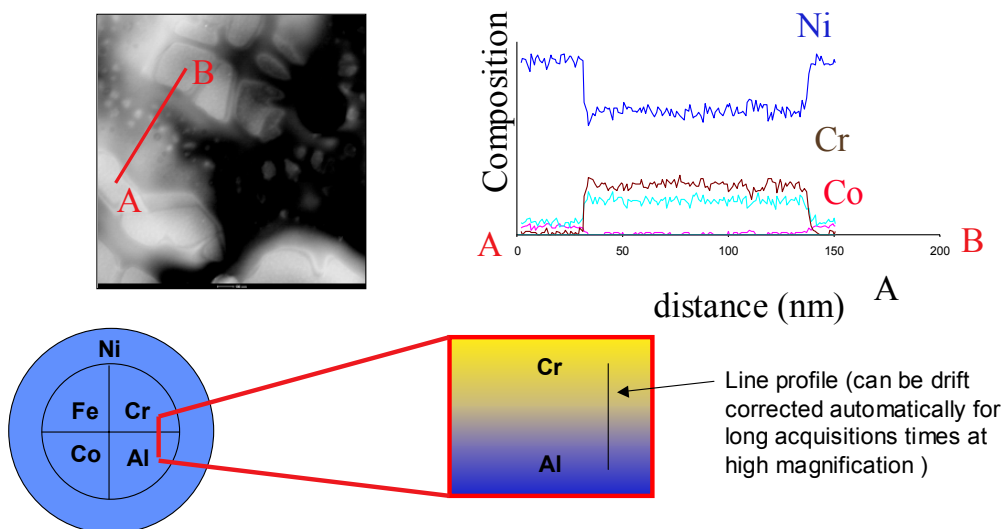
Figure 3. Example of local chemistry profiling that can be combines with the local specimen extraction via FIB.
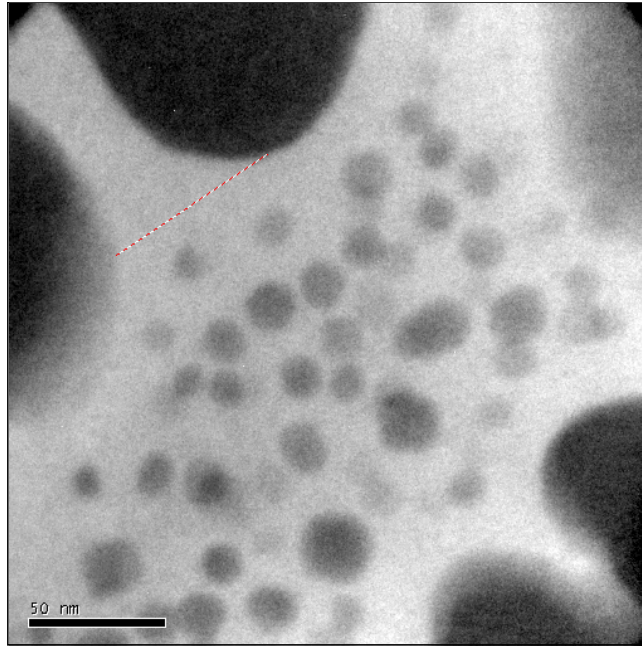
Figure 4. Energy Filtered (EFTEM) With Gatan Imaging Filter demonstrating resolution of the finest tertiary g' precipitates (< 5nm).

The procedure established is now capable of performing the quantity of work required to characterize the diffusion multiple nickel base superalloy samples and support deformation mechanism/structure interactions. Figures 3 and 4 also highlight the capability of the approach. This localized specimen extraction when combined with OSU analytical equipment promised to be an exciting, integral part of future microstructural and deformation studies.

Further characterization work on quantitative structural studies and additional deformation mechanism samples from other disk life meter tasks will be carried out when funding becomes available

1.3   Subtask 1.1.2 - Superalloy Damage and Failure Mechanisms

1.3.1   Summary

An understanding of the deformation mechanisms that are operative during long, hot hold times during an engine mission is critical for being able to predict the damage accumulation in a component of the Intelligent Engine.

1.3.2   Background

The combination of a robust damage model and temperature/stress sensor data is required for path dependent damage prediction, which would be a component of the Disk Life Meter used to periodically calculate the remaining life of a turbine disk. In this subtask, the GEAE, NASA, and OSU team has applied advanced

analytical techniques to characterize damage accumulation and failure modes associated with creep deformation, and assessed methods of temperature sensing for on-wing Disk Life Meter predictions.

In order to allow OSU to characterize material which has experienced creep damage representative of the desired long, hot hold time missions, GEAE and NASA provided eight interrupted creep specimens of supersolvus R104 nickel-based superalloy at a variety of stresses and temperatures, with accompanying electronic creep strain – time data for each specimen. Also, NASA supplied baseline R104 characterization data as a template/starting point for OSU analytical work. The characterization plan OSU has used during this task paralleled prior work done on René 88 DT (R88DT) alloy under the DARPA AIM program.

The samples that were examined and their characterization are shown in the table below.

Specimen ID	Stress, KSI	Temperature, deg F	TEM Analysis	Mean secondary γ' size, nm	Mean tertiary γ' size, nm
8505-C4	100	1250	Complete	159.49	in process
1959-C6	100	1250	Complete	216.78	20
H111-C10	105	1300	Complete	190.43	20
S110-C3	60	1300	Complete	307.79	62
1958-C4	50	1400	Complete	227.23	in process
1959-C4	50	1400	Complete	187.89	NONE
H101-C4	50	1500	in process	255.6	NONE

Table 1 Status of R104 specimens selected for creep mechanism characterization

1.3.3 Creep specimen characterization

Characterization of the gamma prime (γ') size populations is required for the validation of the microstructural evolution model for γ' in the AIM precipitation models. The precipitate size populations are inputs to the AIM creep model, as the operation of the creep mechanisms depends on the interaction of dislocations with the material microstructure. Secondary γ' sizes were characterized, and tertiary γ' measurements are largely complete; OSU will complete the remainder for their final report.

The key observation made from these new tertiary measurements is that the tertiary γ' is absent in the specimens tested at 1400F and 1500F. Tensile specimen ends are being evaluated now that were taken from locations near these creep specimen locations, to evaluate the starting microstructure. TEM

work conducted on tensile bar ends at the same forging location indicates that the tertiary γ' is in existence at those locations before the creep testing. This would mean that at 1400F and greater temperatures, the tertiary γ' has gone into solution, and can no longer play a role in the mechanical behavior of the alloy. Future work will be required to validate models that can predict the rate of coarsening or cautioning of the tertiary precipitates.

The results of the Energy-Filtered TEM work completed by OSU on the provided creep specimens are shown summarized in Figure 1. The predominant mode of deformation observed was the "micro-twinning mode", which was recently discovered to be operative in similar temperature and stress ranges in R88DT in the DARPA AIM program. This mechanism is very different from the dislocation bypass, or climb and glide, mechanism operative at higher temperatures (1400-1500F). One can see that the transition between these two mechanisms coincides with the dissolution of the tertiary γ' above 1400F during the creep test. Future creep work should include investigation of testing at higher stress levels, in order to further validate the existence of Dislocation Looping and Isolated Faulting mechanisms that were observed on R88DT under similar temperature-stress conditions.
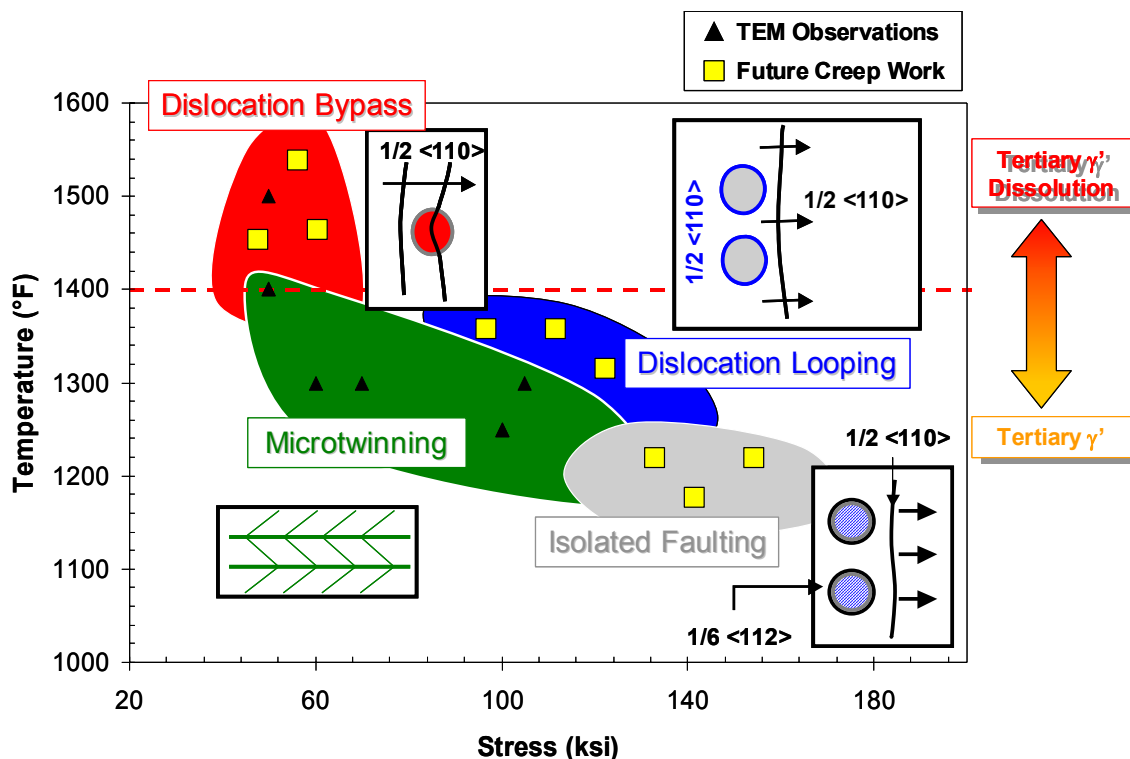
Figure 5 Schematic showing the identified and predicted creep deformation mechanism regions in temperature-stress space.

The results of this work are particularly important for understanding the types of microstructural damage that one might encounter at the tip of a long, hot hold time fatigue crack. Figure 2 shows a schematic of the damage mechanisms that would be expected in the zone near the crack tip. Close to the crack tip, the high-stress mechanisms of Orowan looping or isolated faulting would occur. However, beyond the crack tip, the micro twinning mechanism would be operative.
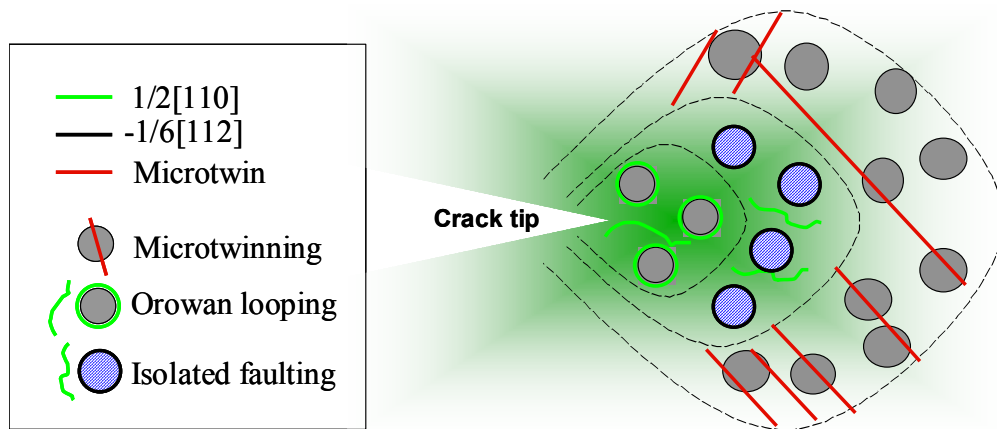
Figure 6 Schematic of the damage mechanisms expected at the crack tip of a fatigue crack with significant hold time.

1.3.4 Future Work

The testing required for an improved creep model that is based on the operative mechanisms observed in R104 was developed during this reporting period. This testing would be initiated when the next year of funding becomes available. The testing matrix, shown in Table 2, would be conducted to determine the key model parameters in the dislocation velocity term for diffusion-mediated glide during the micro twinning process; the other parameters necessary to determine the strain rate would be obtained from direct TEM measurements:

• Velocity for diffusion-mediated glide (Srinivasan, et al):

$$v_{tp} = \frac{a^2 D_o \pi (\tau_a - \tau_{fric})^n}{kT} \exp\left(-\frac{Q_D}{kT}\right)$$

• Strain rate:

$$\dot{\gamma}_{twin} = (1 - f_2 - f_3)\, \rho\, b\, v_{tp}$$

Key Model Parameters: Obtain from transient creep experiments

D_o	Diffusion coefficient	n	Exponential factor
τ_{fric}	Friction flow strength	Q_D	Activation energy of diffusional process

Microstructure Parameters: Obtain from direct TEM measurements

$f_2\ f_3$ Volume fraction of secondary/tertiary γ' ρ Dislocation density

Figure 7 Creep model developed for R014.

Table 2. Proposed creep testing in Phase II of the IPSFT Disk Life Meter Task 1.1.2.1.

Creep Testing Alloy	Stress State	Cooling Rate F/min	Test Temperature	Test Temp 2 (optional)	Stress ksi	Stress 2 ksi (opt.)	Strain level of change	Strain level to interupt
Rene104	tension	use AIM to give same structure as R88DT	1200	T2- 1300	105		0.10%	0.20%
Rene104	tension	75F/min	1200	T2 - TBA	105		0.10%	0.20%
Rene104	tension	75F/min	1200		105	114	0.10%	0.20%
Rene104	tension	75F/min	1200		105			0.20%
Rene104	tension	75F/min	reserve					0.20%
Rene104	tension	75F/min	reserve					0.20%
Rene104	tension	400F/min	1200	T2- 1300	121		0.10%	0.20%
Rene104	tension	400F/min	1200	T2- TBA	121		0.10%	0.20%
Rene104	tension	400F/min	1200		121	141	0.10%	0.20%
Rene104	tension	400F/min	1200		121			0.20%
Rene104	tension	400F/min	reserve					0.20%
Rene104	tension	400F/min	reserve					0.20%
Rene104	compression	400F/min	1200		121			0.20%
Rene104	compression	400F/min	1200		121			0.20%
Rene104	compression	400F/min	reserve					
Rene104	compression	75F/min	1200		105			0.20%
Rene104	compression	75F/min	1200		105			0.20%
Rene104	compression	75F/min	reserve					

In addition to the specimens above, Hold Time Fatigue Crack Growth specimens from the NAI VAATE program may be analyzed using the FIB procedure

developed during the Disk Life Meter program to verify the deformation mechanisms occurring during hot, long-hold-time fatigue damage. This work will provide a crucial link between the creep and fatigue deformation, and provide the basis for model verification for the deformation mechanism component of the Disk Life Meter.

Temperature sensors were investigated for their applicability to on-wing rotating applications during this study, such that the Disk Life Meter could contain a temperature-path-dependent model and predict real-time the remaining creep life in a component. While pyrometry or sensing of thermographic phosphors hold much promise for test engine temperature sensing, the supporting signal processing equipment would pose a significant weight penalty. Other options include embedded electronics or magnetics; however these technologies are still in the development stages for components that will survive the harsh conditions of the engine and be able to transmit an RF signal that will not be influenced by background noise and rotation. In Phase II of the Disk Life Meter Task 1.1.2.1, we will downselect and incorporate one of these temperature-sensing techniques in our creep tests in order to test its long-term stability.

1.4 Subtask 1.2.2 - Superalloy Hot Corrosion

1.4.1 Summary

Laboratory testing confirmed that a four-component sulfate derived from field service inspection could repeat the corrosion experience on turbine disks and seals. This sulfate mix is deposited by impact during engine operation and forms a basic layer on the surface of the component. Sulfides formed by reaction with the substrate increasing basicity and promoting a protective oxide dissolution and reprecipitation mechanism that is indicative of Type I corrosion. A temperature study confirms that the corrosion only occurs above the eutectic temperature of the four-component sulfate. Methods were evaluated to reduce the corrosion potential of the sulfate mix. The formation of a protective Al_2O_3/Cr_2O_3 surface oxide by preoxidation may have been effective except that a thermal exposure greater than 1300°F for 48 hours in a H_2/H_2O atmosphere was necessary to form a sufficient scale. A CeO_2 protective layer did show capability in limiting the reaction of the four-component sulfate with the substrate if the coating was adherent and continuous.

1.4.2 Background

Hot corrosion of gas path turbine engine components has been known for the last 50 years. This corrosion has been well studied and two general classes of hot corrosion have been used to categorize the observed corrosion. Type I hot corrosion occurs at high temperatures when Na_2SO_4 (also other sulfates, carbonates, etc.) condenses onto components and causes a liquid salt fluxing

with the alloy [1]. Type II occurs at temperatures below the salt melting temperature where sulfur oxide gases are present and forms a low melting $Na_2SO_4/CoSO_4$ or $Na_2SO_4/NiSO_4$ eutectic [2]. Recently, General Electric (GE) turbine engines have exhibited evidence of hot corrosion type pitting in non-combustion path cooling circuits. The parts susceptible to this new regime of corrosion are turbine disks and seals in the high-pressure turbine section.

The advanced engine disks and seals are made from a variety of forged structural alloys including the most recent high strength powder processed isothermal forged disks. Since the components are not exposed to the combustion path gases that contain $O_2/SO_2/SO_3$, they cannot be susceptible to the expected Type II corrosion that would be expected at this temperature range. In addition, the salt is supplied by ingested dirt traveling through cooling circuits. The "engine dirt" is a compilation of runway dirt, fly ash, concrete dust, sea salt, etc. as oppose to NaCl that is converted to the traditional Na_2SO_4 by the sulfur in the jet fuel. Field service has shown that this "engine dirt" collects on the corrosion prone parts.

Figure 8 is a cross-section structural schematic of the corrosion pitting. It can be seen that nickel sulfides are formed underneath a porous non-protective cobalt/nickel oxide. Sulfides are a known characteristic of Type I corrosion that form when the sulfate rich salt reacts with the metal substrate increasing the dissolution of the protective oxides.
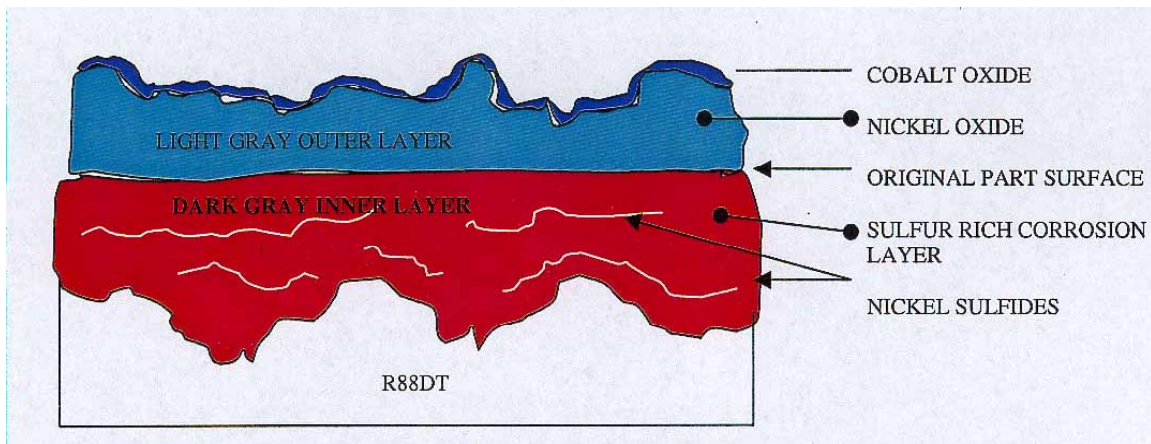
Figure 8: Schematic of the corrosion layers seen in field service HPT disk and seals.

From the information known, Type II corrosion is unlikely in this case, but Type I corrosion has never been reported in the literature at temperatures this low. A mechanistic understanding of the corrosion is needed to address the problem affectively.

1.4.3 Four-Component Sulfate

From the metallography completed on corroded field service parts, nickel sulfides were shown to be present. This is a well-known characteristic of Type I corrosion, but Type I corrosion does not occur below the liquidus of the salt film. Previously, GE conducted differential thermal analyses (DTA) on samples of actual "engine dirt" extracted from field service parts. It was shown that the dirt had a eutectic between 1076-1292°C (580-700°C) with final melting temperatures around 1292-1472°C (700-800°C) (Na_2SO_4 melting temperature = 884°C). In addition, a chemical analysis was completed that showed a variety of sulfates (Ca, Mg, Na, K) as well as a significant amount of silica. The silica indicates that the "engine dirt" is deposited by impact instead of condensation.

An accurate corrosion salt was needed to conduct laboratory testing. According to the previous GE wet chemistry analyses of three engine lines, the original salt deposit responsible for hot corrosion is a four-component sulfate: $CaSO_4$- $MgSO_4$- Na_2SO_4- K_2SO_4. From the analyses for elements Ca, Mg, Na and K, the compositions of their sulfates were calculated, and a representative composition of the four-component sulfate was chosen for experimentation, as shown in Table 2.

Table 2: Calculated composition of the four-component sulfate

Available data of elements		Calculated composition of sulfates		
Element	Relative proportion of the four elements	Sulfate	Composition Wt %	Representative composition, wt %
Ca	62.47	$CaSO_4$	60.83	60
Mg	15.48	$MgSO_4$	21.97	20
Na	12.60	Na_2SO_4	11.16	15
K	9.45	K_2SO_4	6.04	5

The eutectic point of this four-component sulfate was determined by DTA to be ~1216°F (658°C), as seen in Fig. 1. The sample used for the DTA was premelted at 1300°F (704°C) prior to testing.
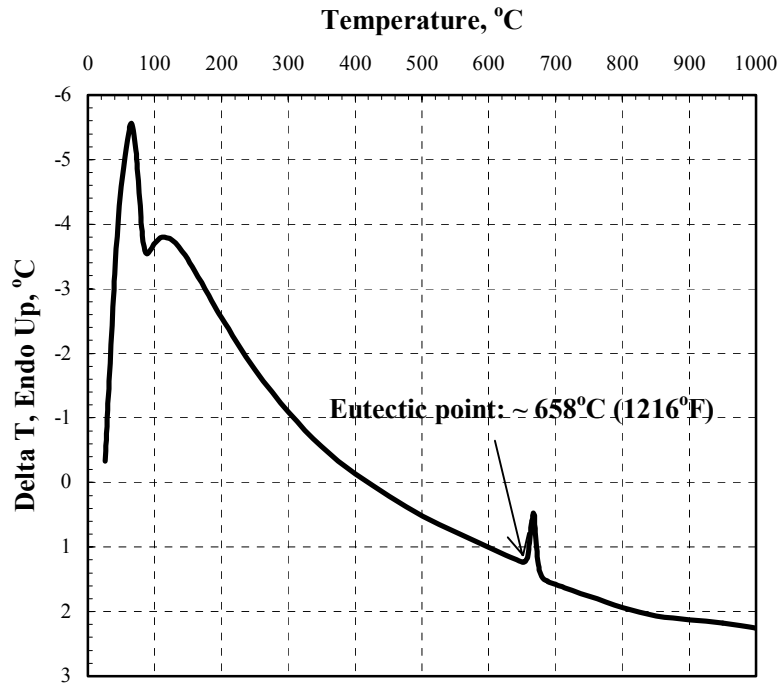
Figure 9: DTA analysis result for the four-component sulfate.

This four-component sulfate appears to be an accurate representation of the "engine dirt" seen on field service parts.

1.4.4 Hot Corrosion Tests on Alloys R88DT and R104

Hot corrosion tests were conducted on R88DT and R104. The alloy specimens were coated with the four-component sulfate salt by brushing a mixture of fine, premelted salt powder with acetone onto warm specimen surfaces, or by dipping warm specimens into a colloidal suspension of salt powder in isopropanol and

then drying under an infra-red lamp. Figure 10 is a schematic illustration of the set-up for the hot corrosion test. Hot corrosion tests were carried out in air at 1300°F for 48 hours. After test, the salt layer on the alloy surface was removed by a water rinse with the use of a soft brush. Then the surface morphologies of the test specimens were observed under a scanning electron microscope (SEM), and energy dispersive spectroscopy (EDS) was also used to analyze elemental compositions in some areas.

Figure 11 shows the surface morphology of a corroded coupon of R88DT. As seen in Figure 11 (a), the salt-coated coupon was subject to hot corrosion. The loose or porous oxide layer on the alloy surface was removed with the salt by the water rinse while some oxide islands remained on the alloy substrate, as clearly shown in Figure 11 (b). Tiny corrosion pits can also be seen in the alloy substrate of Figure 11 (b). Figure 12 (a) and (b) show the EDS analysis results for the oxide island and for the alloy substrate, respectively. Clearly, the oxide island is enriched in Cr, Al and Ti, while the underlying alloy is depleted in the elements but enriched in Ni and Co.
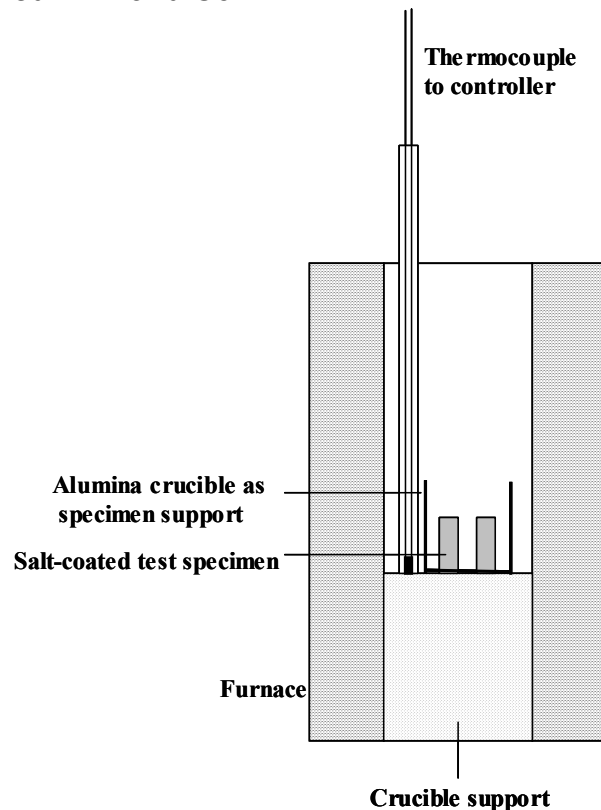
Figure 10: Schematic illustration of the set-up for hot corrosion test.
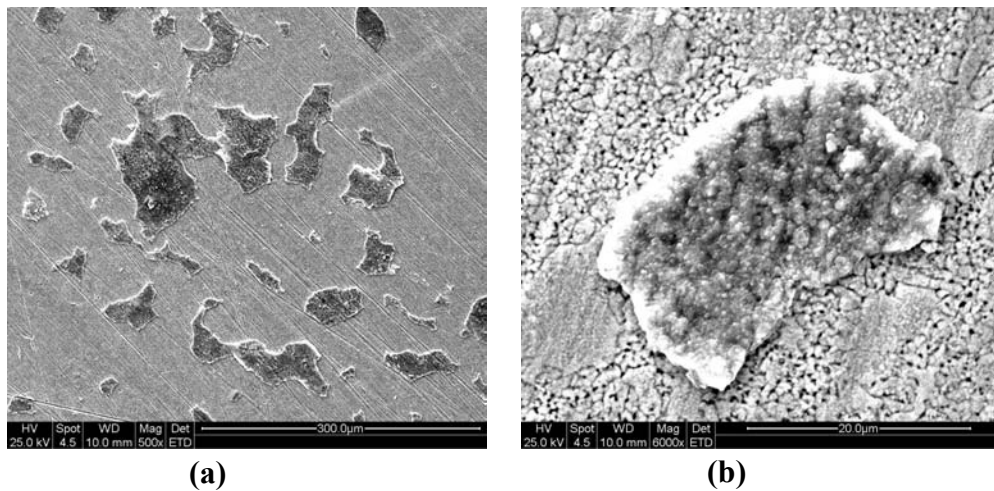
Figure 11: Surface morphology of hot corrosion test coupon of R88DT.

(a)
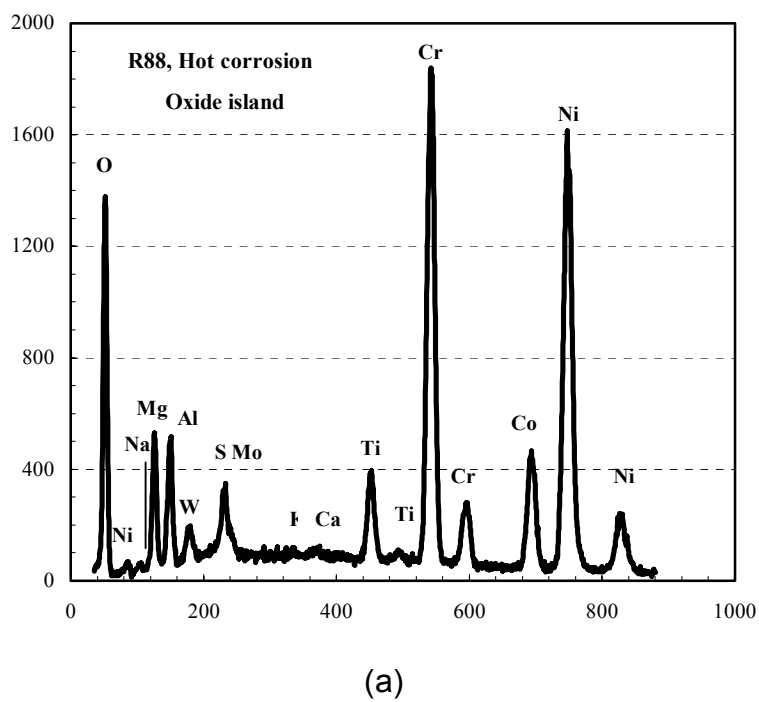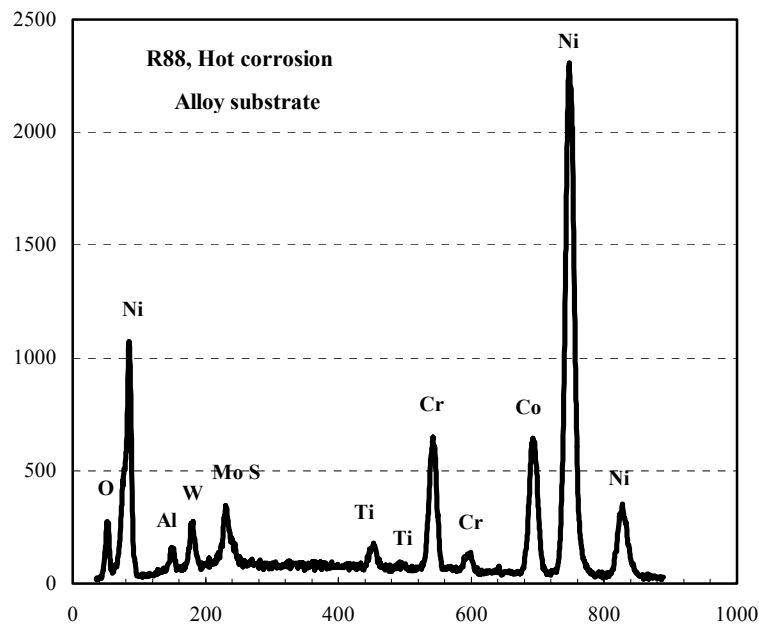
(b)

Figure 12: EDS results for oxide island (a) and for alloy substrate (b) of R88DT.

Figure 13 shows similar surface morphologies for the hot corrosion coupon of alloy R104. The EDS analysis results are also very similar to those for R88DT, and therefore,

(a)   (b)
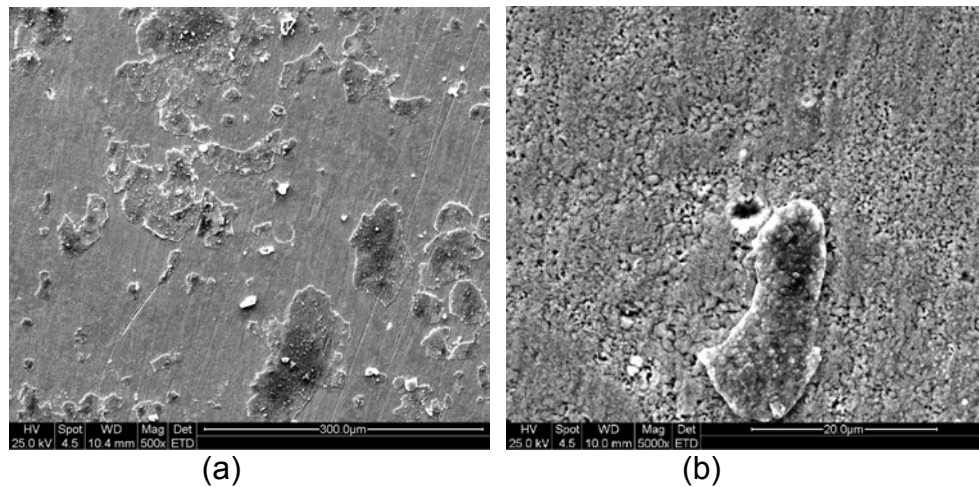
Figure 13: Surface morphology of hot corrosion test coupon of R104.

are not shown here. Again, the EDS results indicate that the oxide islands on the alloy surface were rich in Cr, Al and Ti, compared to the alloy substrate, as shown in Table 3.

Table 3: Ratios of at % (Cr+Al+Ti)/at % (Ni+Co) for oxide island and alloy substrate

Alloy	Ratio of at % (Cr+Al+Ti)/at % (Ni+Co)	
	Oxide island	Alloy substrate
R88DT	0.86	0.19
R104	0.76	0.26

These hot corrosion test results indicate that both alloys were subject to hot corrosion. The corrosion morphology was characterized by a loose (porous) oxide layer mixed with salt, Cr, Al and Ti-rich oxide islands adherent to the alloy substrate, and an alloy substrate with many tiny corrosion pits.

1.4.5 Hot Corrosion Tests at 1200 and 1400°F

To prove the key role of a liquid salt phase in the occurrence of hot corrosion, salt-coated coupons of R88DT and R104 were oxidized in air for 48 hours at 1200°F (below the eutectic point), and 1400°F (above the eutectic point), respectively. As seen in Figure 14, the salt coatings on the alloy coupon surfaces remained solid (not melted) in 1200°F test. After the salt coatings were removed by a water rinse, the underlying alloy surfaces still looked a little shiny, which implies that the salt-coated coupons underwent even less oxidation than uncoated ones, because the solid salt coating acted as a barrier to oxygen supply to the alloy surface. No oxide was removed during salt rinse indicating an adherent uncorroded oxide.
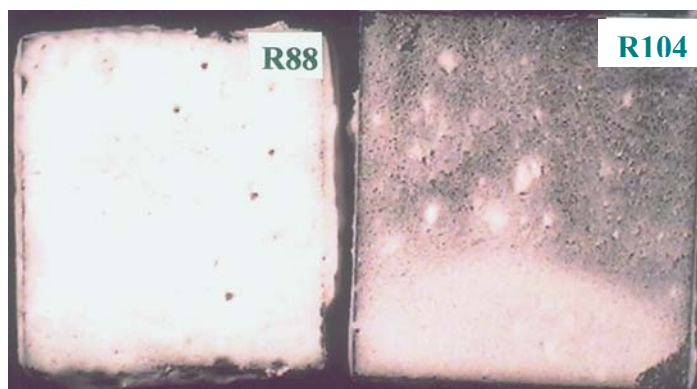
Figure 14: Appearance of the salt coatings on the alloy surfaces after test

At 1400°F, the four-component sulfate caused severe hot corrosion attack of the two alloys. The weight gains were measured (for the alloy coupons with a salt coating only on the top side) to be ~1.5 mg and ~ 3.2 mg for each coupon (the top side is ~0.275" x 0.275") for R88DT and R104, respectively. These weight gain values are larger than those for 48 hour test at 1300°F, which were ~1.0 and ~2.0 mg for R88DT and R104, respectively. Black oxide particles, in addition to undissolved salt, were collected from the water used to remove the salt layer (by ultrasonic cleaning). The surface morphologies of the tested coupons are shown in Figure 15 and Figure 16 for R88DT and R104, respectively. As seen in Figure

15 (a), the salt-coated coupon was subject to hot corrosion. The loose or porous oxide layer on the alloy surface was removed with the salt by the water rinse while some oxide islands adhered to the alloy substrate, as clearly shown in Figure 15 (b).

(a)   (b)
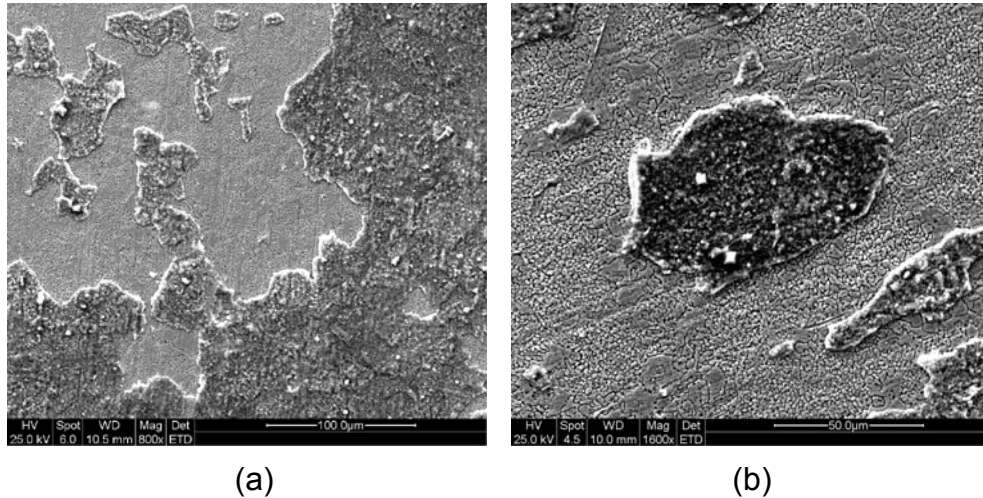
Figure 15: Surface morphology of 1400°F hot corrosion test coupon of R88DT.

(a)   (b)
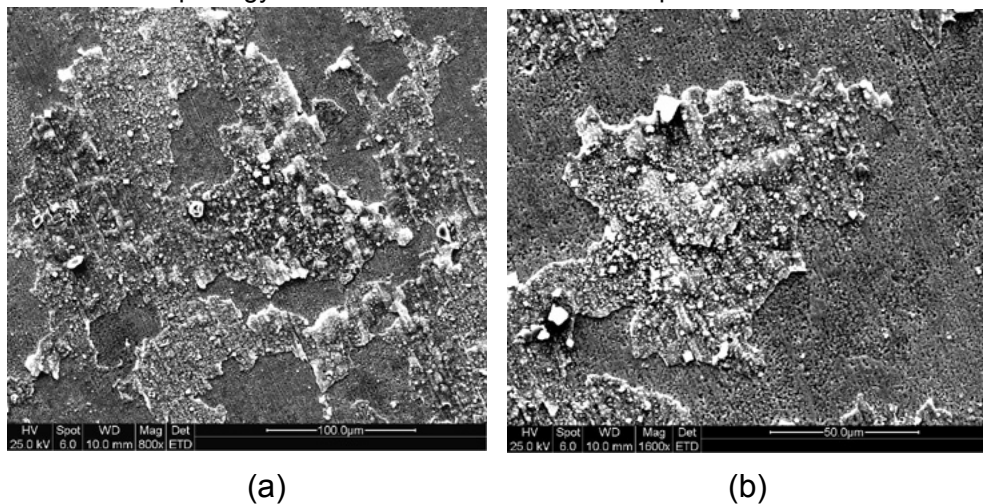
Figure 16: Surface morphology of 1400°F hot corrosion test coupon of R104.

Figure 16 shows similar surface morphologies for the tested coupon of R104. EDS analysis results for the oxide island and for the alloy substrate were conducted as previously. For both alloys, the oxide island is enriched in Cr, Al and Ti, while the underlying alloy is depleted in the elements, but enriched in Ni and Co. These results are similar to corrosion testing at 1300°F.

1.4.6 Long-Term Hot Corrosion Tests

Long-term hot corrosion tests were conducted on the four-component sulfate salt-coated alloy coupons of the R88DT and R104 at 1300°F for 5 days (120 hours). After the tests, the un-reacted salt and black loose corrosion products were removed into water by ultrasonic cleaning. The surfaces of the tested coupons were observed by SEM, and the elements were analyzed by EDS.

(a) (b)
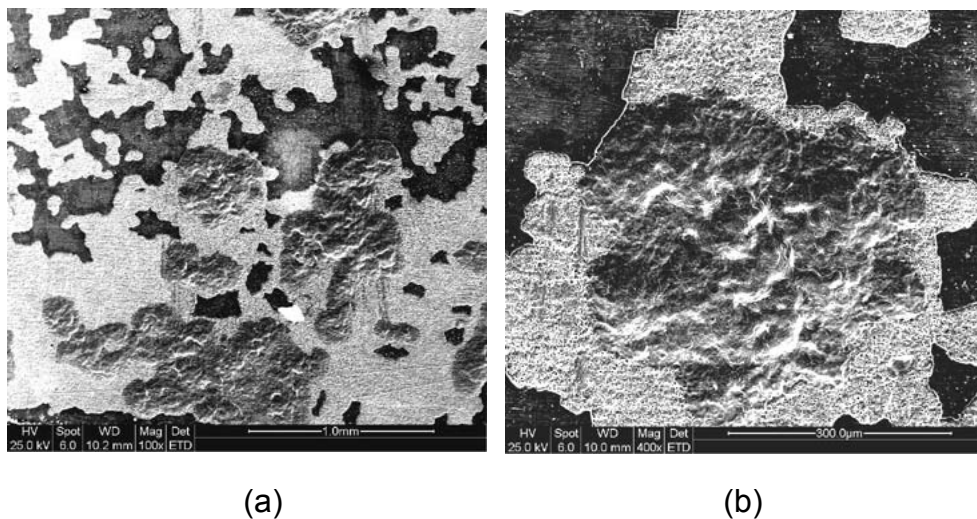
Figure 17: Surface morphology of hot corrosion test (1300°F for 120 hours) coupon of R88DT.

Figure 17 (a) shows the surface morphology of the tested coupon of R88DT. The black areas in Figure 17 (a) are oxide islands, and the lighter areas are alloy substrate. A few quite large corrosion pits can be seen, which are a deeper than the alloy substrate. An enlarged corrosion pit is shown in Figure 17 (b). The surface morphology of the tested coupon for R104 is similar to that for R88DT, and is shown in Figure 18(a) and (b).

(a) (b)
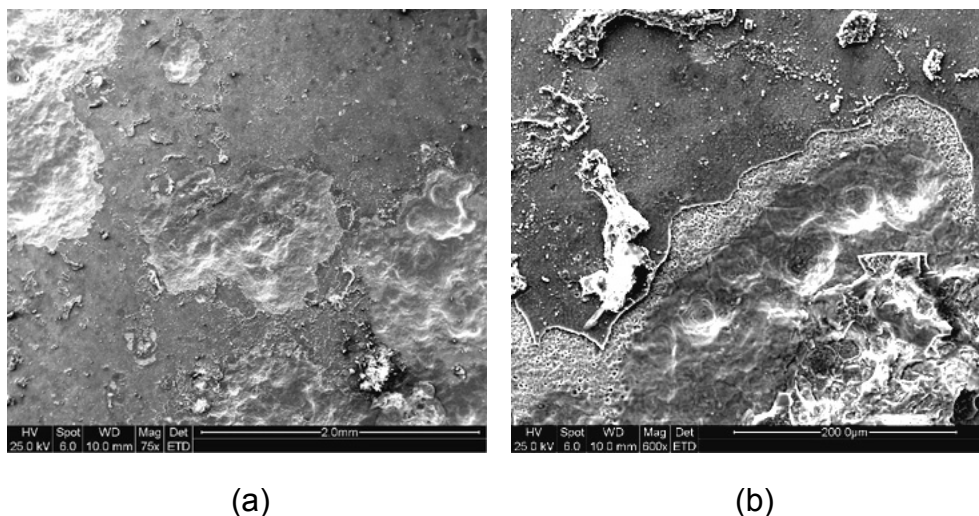
Figure 18: Surface morphology of hot corrosion test (1300°F for 120 hours) coupon of R104.

Figure 17 and Figure 18 indicate that both alloys were subject to non-uniform (localized) hot corrosion attack, in the form of pits.

The EDS results for the tested coupon of R104 are shown in Figure 19 (a), (b), and (c) for the oxide island, the alloy substrate and the corrosion pit, respectively. From these
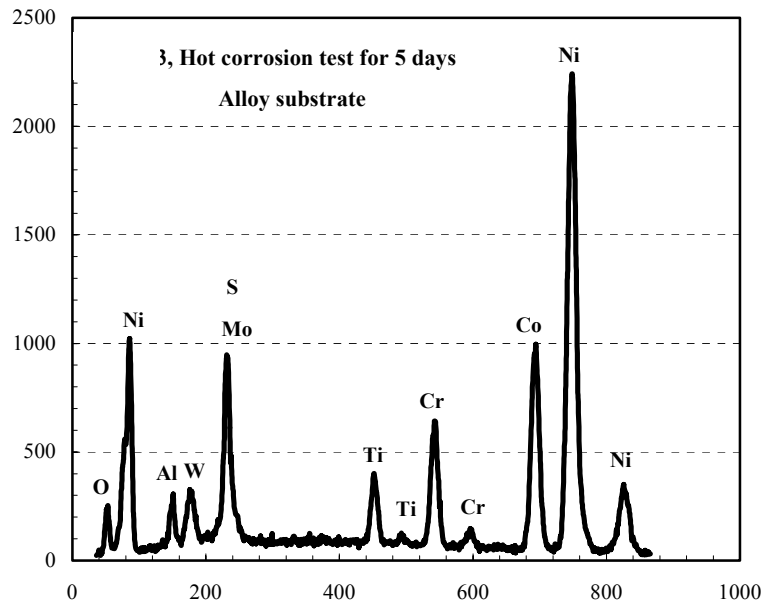
(a)
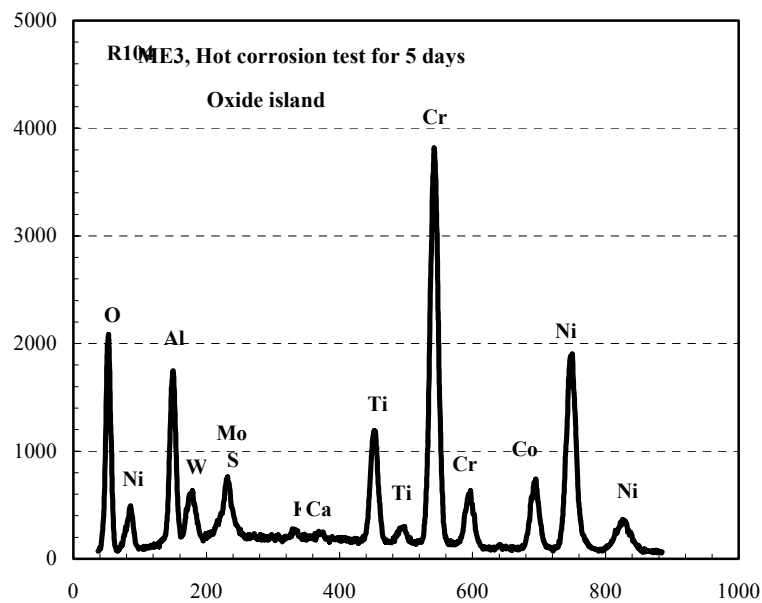
(b)
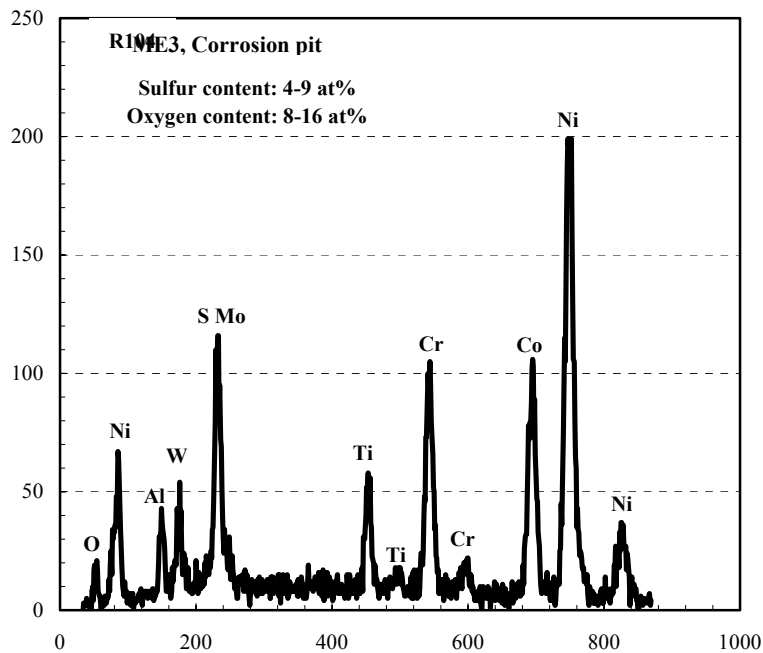
(C)

Figure 19: EDS analysis results for the hot corrosion test (1300°F for 120 hours) coupon of R104.

figures, the oxide island is enriched in Cr, Al and Ti, while the underlying alloy substrate is depleted in these elements, as seen in Table 4.   Higher sulfur content, 4-9 at %, was found in the corrosion pits, compared to 2-3 at % in the alloy substrate of the tested coupon. This high sulfur content in the corrosion pits implies internal sulfidation accompanying hot corrosion.

Table 4 lists the weight gains for the alloy coupons with salt coating only on the top side (~0.275" x ~0.275") after 120 hours of hot corrosion test. These weight-gain values are higher than those for the coupons after 48 hours of hot corrosion. From the weight-gain results for both 48 hours and 120 hours of tests, the hot corrosion resistance of alloy R88DT is better than alloy R104.

Table 4: Hot corrosion test results for alloys R88DT and R104 at 1300°F for 120 hours

Alloy	Weight gain mg/coupon	Ratio of at % (Cr+Al+Ti)/at % (Ni+Co)	
		Oxide island	Alloy substrate
R88DT	1.4	1.8	0.25
R104	2.4	1.4	0.24

1.4.7 Discussion of Hot Corrosion Mechanism

As negligible SO_3 is present in the cooling air service environment, the possibility of occurrence of Type II (so-called low temperature hot corrosion) is eliminated. Because the test temperature of 1300^oF (704^oC) is higher than the eutectic point of the four-component sulfate of 1216^oF (649^oC), the hot corrosion of the alloys would be categorized as Type I hot corrosion (occurring above the salt eutectic temperature). Likewise, because both the service and test environments consist essentially of air, devoid of SO_3, the Type I hot corrosion mechanism must involve basic fluxing.

1. As a significant content of Si (as SiO_2) was detected in surface deposits on the GE field samples, the salt deposit arises from particle impaction, not from condensation.

2. Through flaws in the protective surface oxide, the four-component sulfate reacts with the metal substrate to form nickel sulfides. This reaction increases the basicity of the sulfate mix.

3. High basicity corrodant begins to dissolve protective surface oxides (Al_2O_3, Cr_2O_3, TiO_2, etc.).

4. Dissolved oxides transport down concentration gradient to surface of the corrodant and reprecipitate as non-protective islands of oxide.

5. The substrate is left with high concentrations of nickel and cobalt that from non-protective porous oxides on the surface that do not slow corrosion.

In the current case, hot corrosion of alloys R88DT and R104 was caused by the basic fluxing and reprecipitation of oxides, as proposed by Goebel and Pettit (3) (see
Figure 20), and explained in detail by Rapp et al. (1,4).
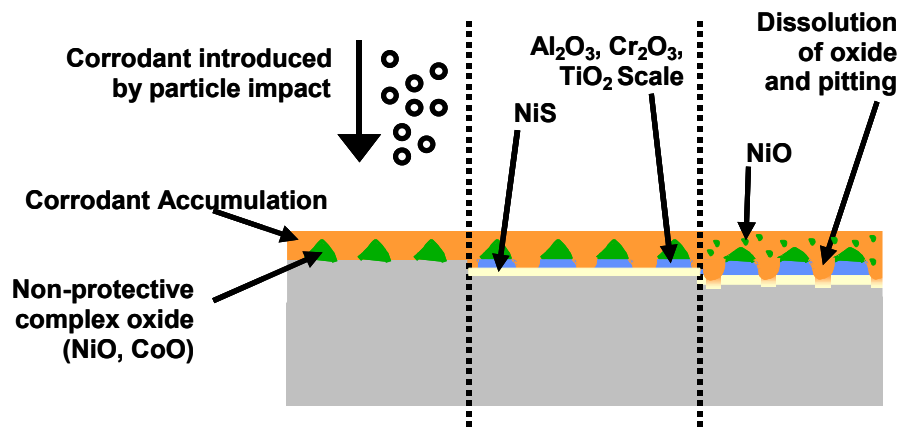
Figure 20: Proposed turbine disk hot corrosion mechanism.

1.4.8 Preoxidation of R88DT and R104 and Its Effect on Hot Corrosion Behavior

With a proposed corrosion mechanism, methods were attempted to reduce or eliminate the corrosion rate of the substrate. It was hypothesized that if a protective Al_2O_3/Cr_2O_3 could be formed prior to deposition of the four-component sulfate, preventing the sulfate/alloy contact would significantly reduce the corrosion rate.

R88DT and R104 coupons were preoxidized in air at 1300°F (704°C) for 48 hours. After preoxidation, the surfaces of the alloy coupons became dark gray. The total weight gain was ~ 0.2 mg for each coupon. Figure 21 (a) and (b) show the surface morphology of the preoxidized R88DT and R104 coupons, respectively. The EDS analysis results for preoxidized R88DT and R104 are similar, and therefore, only the result for preoxidized R88DT is shown here in Figure 22.

The preoxidized R88DT and R104 alloy coupons were coated with the four-component sulfate and subjected to hot corrosion test in air at 1300°F (704°C) for 48 hours. Based on surface morphology observations, as shown in Figure 23 and Figure 24 for tested R88DT and R104, respectively, the preoxidation in air did not offer protection for the alloys. From Figure 23 and Figure 24, the loose (porous) oxide layer (mixed with salt) on the alloy surface was removed during ultrasonic cleaning in water, and some oxide islands remained on the alloy surface, as seen from the hot corrosion test coupons of the bare alloys. Tiny corrosion pits were also seen in the alloy substrate. From the water used to remove the salt layer, black oxide particles were collected, in addition to undissolved salt powder. These black oxide particles are certainly the porous oxide layer removed from the alloy surface.
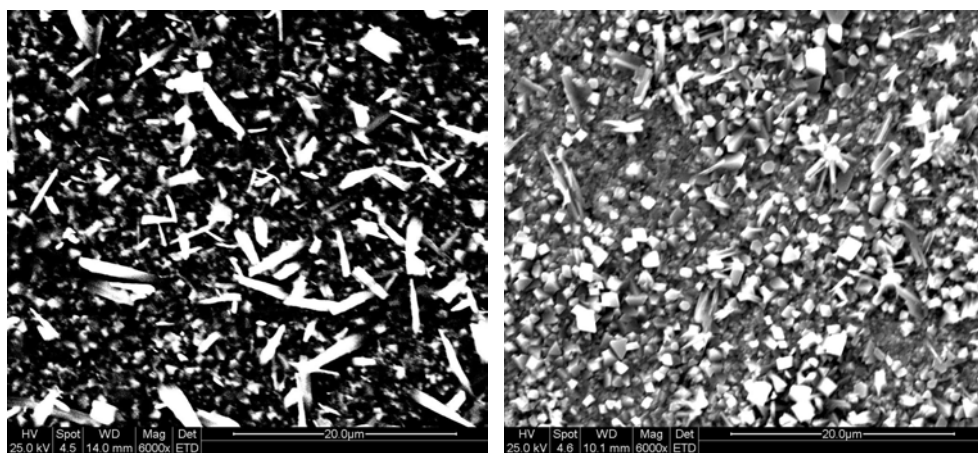
(b)

Figure 21: Surface morphology of R88DT (a) and R104 (b) preoxidized in air.
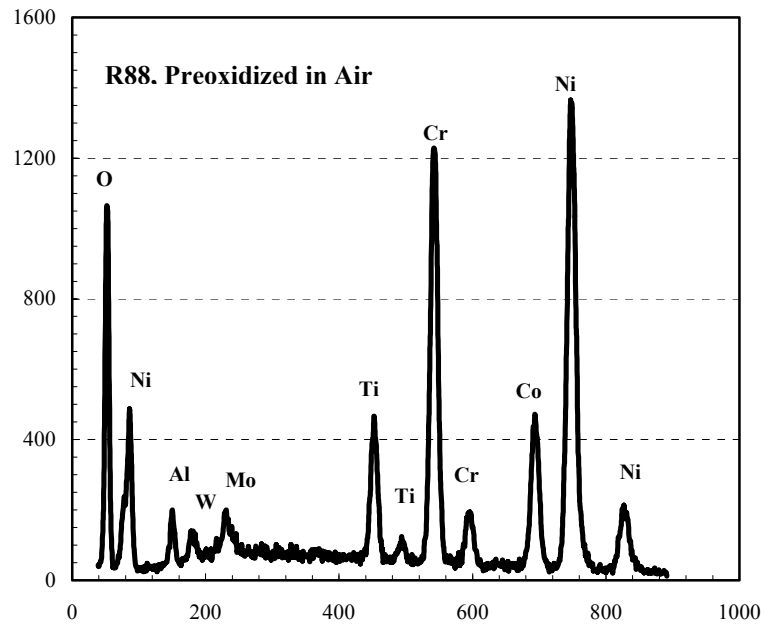
Figure 22: EDS analysis result for R88DT coupon preoxidized in air.
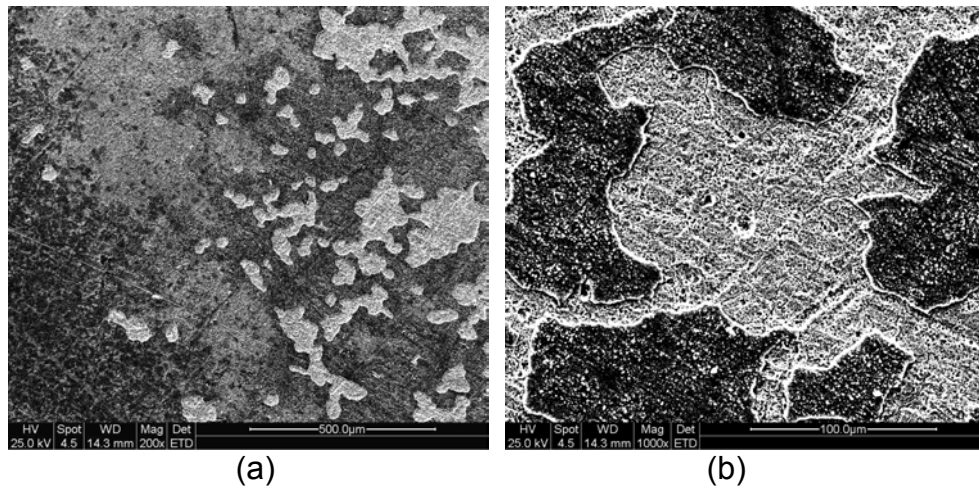
Figure 23: Surface morphology of air-preoxidized R88DT coupon after hot corrosion test: (a) lower magnification and (b) higher magnification.

(a)   (b)
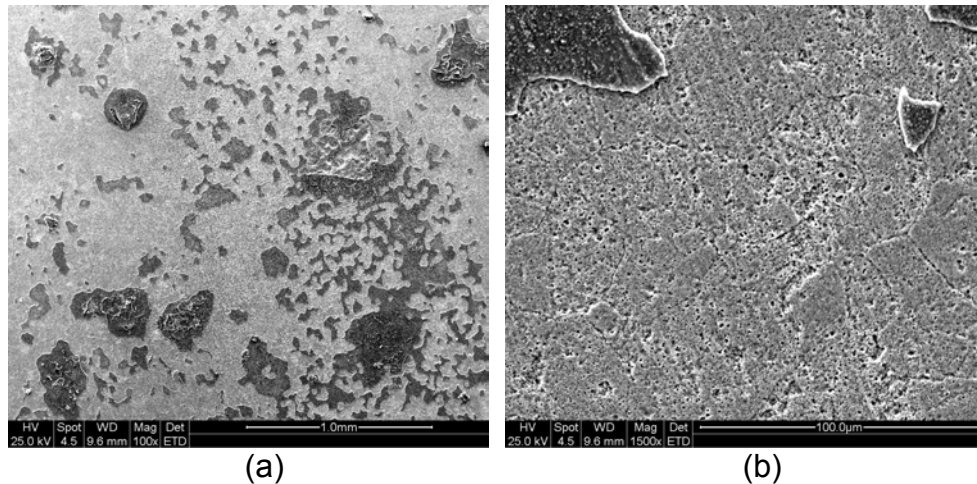
Figure 24: Surface morphology of air-preoxidized R104 coupon after hot corrosion test: (a) lower magnification and (b) higher magnification.

Additionally, R88DT and R104 coupons were preoxidized in tank argon (Argon) at 1300°F (704°C) for 48 hours. The oxygen content in the Argon stream was 50 – 60 ppm as detected by a zirconia oxygen sensor inserted in the reaction chamber for the preoxidation. After preoxidation, the surface color of the alloy coupons was not uniform: the upper part was light gray and lower part was dark gray. The total weight-gain was ~ 0.1 - 0.2 mg for each coupon. Figure 25 (a) and (b) show the surface morphology of the preoxidized R88DT and R104 coupons, respectively. The EDS analysis results for preoxidized R88DT are shown in Figure 26.

(a)   (b)
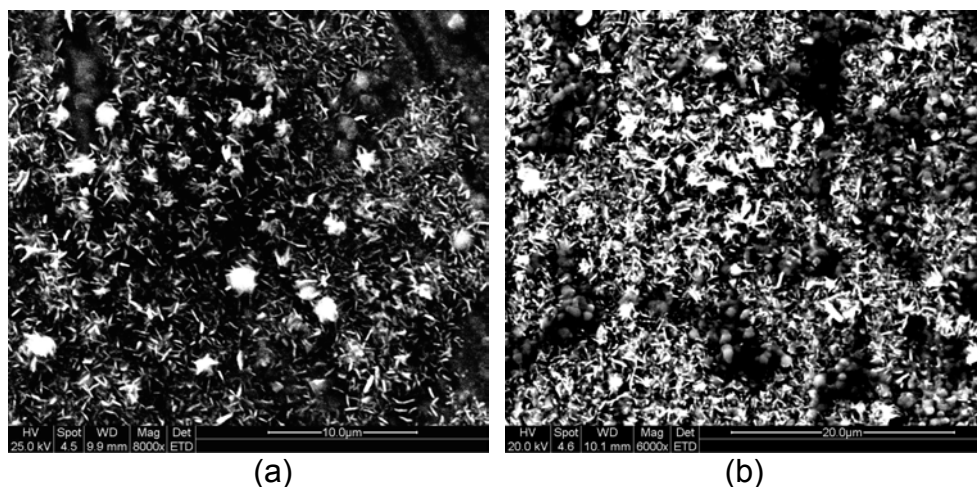
Figure 25: Surface morphology of R88DT (a) and (b) R104 preoxidized in Argon.
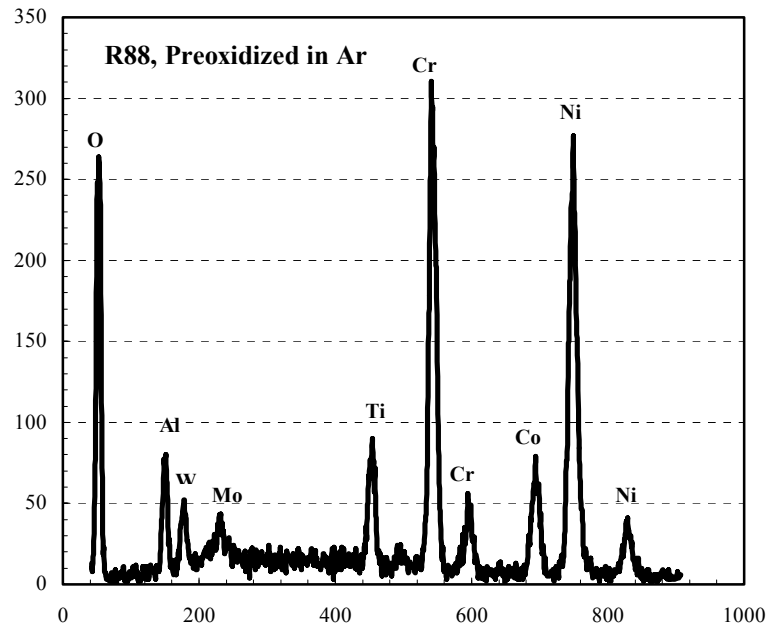
Figure 26: EDS result for R88DT coupon preoxidized in Argon.

The Argon preoxidized R88DT and R104 alloy coupons were coated with the four-component sulfate and subjected to hot corrosion in air at 1300°F (704°C) for 48 hours. Scratches were scribed onto some preoxidized coupons before the hot corrosion test. After the hot corrosion test, the salt layer of the test coupon was removed in water by ultrasonic cleaning
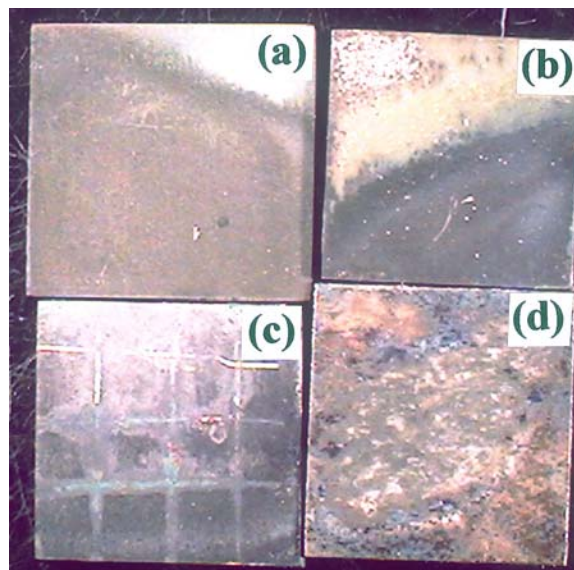
Figure 27: Optical pictures for surface morphologies of as preoxidized coupon (a), hot corrosion test coupon (b), hot corrosion test coupon with scratches (c), and hot corrosion test coupon without preoxidation (d), for R104.

Figure 27 shows low-magnification optical pictures of surfaces for the as-preoxidized coupon (a), a hot corrosion test coupon (b), a hot corrosion coupon with scratches (c), and a hot corrosion test coupon without preoxidation (d), for alloy R104. Similar behavior for alloy R88DT was observed, and is not shown here. Figure 27 also shows that preoxidation in Argon provided partial protection for both alloys, but could not eliminate hot corrosion. Slight hot corrosion occurred to the Argon-preoxidized alloy coupons (b) and (c), compared to the hot corrosion test coupon without preoxidation (d). For the test coupon without preoxidation, the oxide layer was removed from most of the alloy surface (d), while for the test coupons preoxidized in Argon, oxides were detached from only some areas, in particular, the upper part or the edges (b) and (c). A few black oxide particles were also collected from the water used to remove the salt layer, but less than for the hot corrosion test coupons preoxidized in air.

If a comparison is made for the compositions of surface oxide layers of the air-preoxidized and Argon-preoxidized alloys, as shown in Figure 22 and Figure 26, the benefit from preoxidation in Argon may be explained. Table 5 shows that the elements Cr, Al and Ti are richer in the oxide layers for the Argon-preoxidized coupons than for the air-preoxidized coupons. This implies that the lower oxygen content in Argon may hinder the formation of the oxides of base metals Ni and Co, which exhibit lower thermodynamic stability.

Table 5: Ratios of at % (Cr+Al+Ti)/at % (Ni+Co) for surface oxide layers of the alloy coupons preoxidized in air and in Argon

Alloy	Ratio of at % (Cr+Al+Ti)/at % (Ni+Co)	
	Preoxidized in air	Preoxidized in Argon
R88DT	0.61	0.90
R104	0.50	1.02

R88DT and R104 alloy coupons were also preoxidized in a H_2/H_2O atmosphere at 1300^oF for 48 hours. The tank hydrogen gas was introduced into the reaction chamber through a water pool, which was kept at 160^oF throughout the preoxidation treatment. The oxygen partial pressure was measured by an oxygen sensor to be 5.8×10^{-20}-6.3×10^{-19} atm., which is lower than that for the formation of NiO and CoO at 1300^oF (included pO2 for NiO and CoO formation). After preoxidation, the alloy coupons became quite dark, but almost no weight change was measured. The surface morphologies of the preoxidized coupons of R88DT and R104 are shown in Figure 28 (a) and (b), respectively. The oxide layers formed on the alloy surfaces looked very thin, and the low stress grinding marks formed during the sample preparation were clearly seen.

(a)   (b)
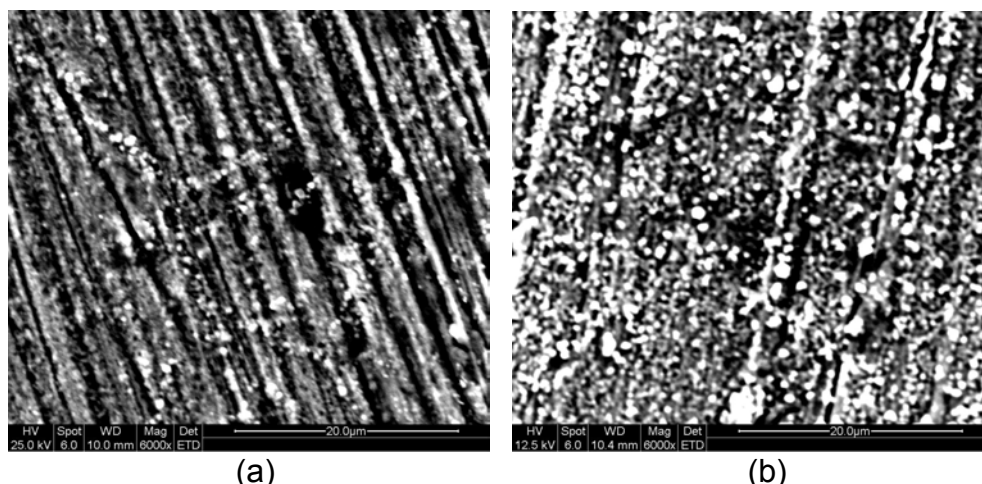
Figure 28: Surface morphology of R88DT (a) and R104 (b) preoxidized in H2/H2O.

An EDS analyses were performed at accelerating voltages of 12.5, 15, 20 and 25 kV. The ratios of at % (Cr+Al+Ti)/at % (Ni+Co) are shown in Table 6 as a function of accelerating voltage. As the oxide film was very thin, the electron beam probably could penetrate into the alloy substrate. Therefore, the elements Cr, Al and Ti may be more enriched than listed in Table 6. The lowest EDS voltage would indicate the more representative composition.

Table 6: Ratios of at % (Cr+Al+Ti)/at % (Ni+Co) vs. accelerating voltage

Alloy	25 kV	20 kV	15 kV	12.5 kV
R88DT	0.47	0.58	1.08	2.05
R104	0.45	0.60	1.10	2.08

Hot corrosion tests were conducted on the preoxidized alloy coupons of R88DT and R104 at 1300°F for 48 hours. The weight gain (with salt coating only on the top side) for preoxidized R88DT was 1.0 mg, while that for preoxidized R104 was 1.9 mg (this is similar to unprotected R88DT and R104). Black oxide particles, in addition to undissolved salt powder, were collected from the water used to remove the salt layer after hot corrosion test. The optical pictures of surface morphologies of the tested coupons in Figure 29 show that the preoxidized alloys underwent hot corrosion attack at temperature. These results indicate the preoxidation in the H_2/H_2O atmosphere did not provide protection from hot corrosion for the two alloys of interest. As described above, the oxide layer formed in the preoxidation treatment was very thin, and may not be perfect. The liquid salt could penetrate through the imperfections and contact the alloy surface and cause hot corrosion. It is also possible that the liquid salt would dissolve the oxides and touch the alloy surface, thus inducing hot corrosion of the underlying alloy.
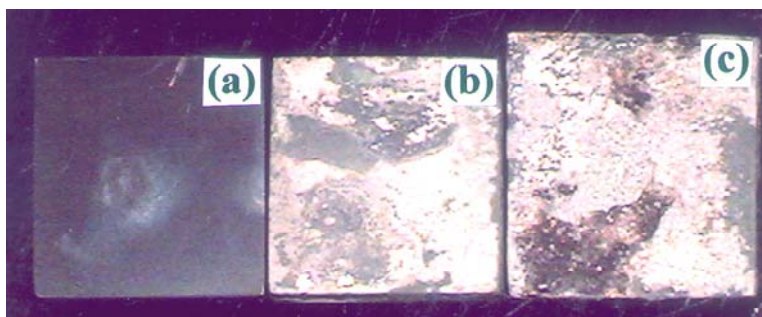
Figure 29: Optical pictures showing surface morphologies of hot corrosion coupons of alloys R88DT and R104 preoxidized in H2/H2O atmosphere (a) R88DT, as preoxidized, (b) R88DT, after preoxidation and hot corrosion, and (c) R104, after preoxidation and hot corrosion.

From this testing it was determined that forming a protective Al_2O_3/Cr_2O_3 that would inhibit corrosion would require pre-oxidation in the H_2/H_2O atmosphere for durations much greater than 48 hours at 1300°F. This is not an economically feasible process for turbine disks and seals.

1.4.9 Cathodic Deposition of CeO_2 and Its Effect on Hot Corrosion Behavior

As discussed previously, the mechanism of hot corrosion caused by the four-component sulfate deposit at temperatures above its eutectic point of 1216°F would be categorized as Type I hot corrosion, involving basic fluxing of the oxide scale. For this reason, a coating of an acidic oxide, e.g., CeO_2, may combat the basic fluxing and provide protection for the underlying alloy. Therefore, preparation of a thin CeO_2 deposit on the alloy surface was tried by cathodic polarization in $Ce(NO_3)_3$ solution, and the effect of the coating was evaluated by hot corrosion test of the coated coupons.

A Pt wire (as lead wire) was connected to the alloy coupon by spot welding. The cathodic polarization was conducted in a 0.2 M $Ce(NO_3)_3$ solution at a potential of E = -1.3V (SCE) for 15 minutes in the first trial. A CeO_2 coating (~5 mg) was obtained after drying the coupon in air and then in an oven at ~ 80°C. In this first trial, the alloy coupons were cleaned only with isopropanol alcohol, i.e., the passive film on the alloy surface was not removed. As a result, the CeO_2 coating was very loose, and some CeO_2 particles fell off the alloy surface during handling.

The four-component salt powder was applied to the topside of the CeO_2-coated alloy coupon, and the hot corrosion test was conducted at 1300°F for 48 hours. The weight gain for each coupon was 0.2 - 0.3 mg, compatible to that for pure oxidation in air. This implies a major improvement over an uncoated hot corrosion test. Unfortunately, the liquid salt was able to penetrate through the

loose CeO$_2$ coating and touch the alloy substrate, thus causing localized hot corrosion.

In the next trial, R104 alloy coupons were first immersed in a mixture of acids HCl, HNO$_3$ and CH$_3$CO$_2$H to remove the passive film before cathodic deposition of the CeO$_2$ deposit. The cathodic polarization was performed for 30 seconds or else 3 minutes. For the coupons with 3 minutes of cathodic polarization, a uniform CeO$_2$ coating was formed and the alloy surface was totally covered although the coating was still loose. But CeO$_2$ particles did not detach from the alloy surface except along the coupon edges. For the pre-cleaned coupons deposited with CeO$_2$ for 30 seconds of cathodic polarization, the CeO$_2$ deposit was adherent and hardly seen.

The CeO$_2$-coated R104 coupons involving 30 seconds of cathodic polarization were preoxidized in air at 1300°F for 48 hours, followed by a hot corrosion test at the same temperature for the same time duration. The coupons so treated were found to be subject to hot corrosion, as seen from Figure 30.

Figure 30: Optical pictures showing surface morphologies of hot corrosion coupons of CeO$_2$-coated (by 30 seconds of cathodic polarization) and preoxidized R104 (a) As preoxidized, (b) after preoxidation and hot corrosion, and (c) after preoxidation, hot corrosion and removing the salt layer.

The CeO$_2$-coated R104 coupons involving 3 minutes of cathodic polarization, without preoxidation, were subjected to the hot corrosion test at 1300°F for 48 hours. The surface morphologies shown in Figure 31 indicate that this CeO$_2$ coating provided protection to hot corrosion attack although the adhesion of the coating to the alloy substrate needs to be improved further. The weight gain of ~0.5 mg for each coupon was a little larger than that for pure oxidation in air, which is believed to result from hot corrosion attack along the coupon edges. Indeed, hot corrosion occurred along edges, as seen from Fig. 12 (c), where the CeO$_2$ deposit had detached. Figure 31 (b) shows the hot corrosion tested coupon before surface cleaning. The white cover on the alloy surface is believed to be unreacted solid salt, CeO$_2$ and some reaction product formed at the test temperature.
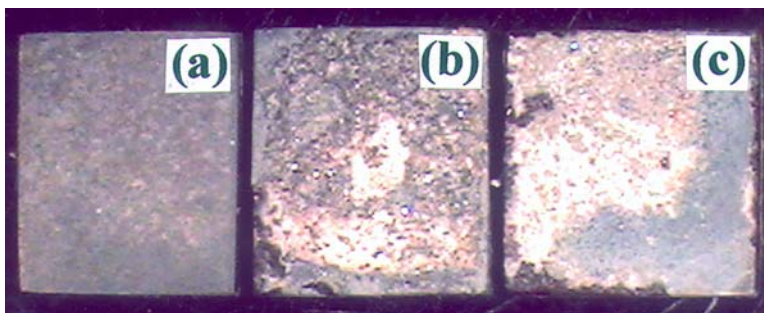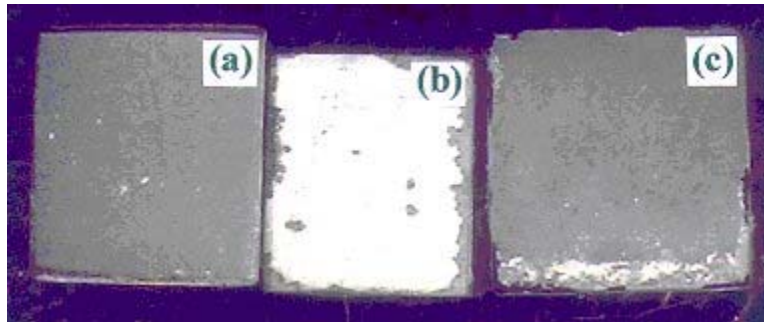
Figure 31: Optical pictures showing surface morphologies of hot corrosion coupons of CeO$_2$-coated (by 3 minutes of cathodic polarization) R104 (a) R104 coupon after pure oxidation in air, (b) after hot corrosion test, and (c) after hot corrosion test and surface cleaning.

In summary, a CeO$_2$ coating is promising in hot corrosion protection for engine disks. The procedure should be improved so that an adherent, dense and continuous CeO$_2$ coating can be produced on the superalloy surface.

1.4.9.1 References

1. R.A. Rapp and K.S. Goto, "Hot Corrosion of Metals by Molten Salts", in Molten Salts, I.J. Braunstein and J. R. Selman, Eds., Electrochem. Soc., Pennington (1981), p. 159.
2. K.A. Luthra and D.A. Shores, J. Electrochem. Soc., 127 (1980), p. 2202.
3. J.A. Goebel and F.S. Pettit, Met. Trans., **1** (1970), p. 1943.
4. N. Otsuka and R.A. Rapp, J. Electrochem. Soc., **137** (1990), p. 46.

1.5 Subtask 1.1.2.3 – Quench Cracking Overview

1.5.1 Summary

GEAE has provided the thirteen on cooling tensile specimens at a variety of strain rates and temperatures and electronic deformation data to enable characterization of the quench cracking that can occur during disk heat treatment to identify the mode of tensile failure. OSU has performed characterization of the specimens and identified different fracture characteristics associated with high versus low ductility regimes. Ongoing characterization of surface characteristics including surface oxidation/oxidation spiking is anticipated to further elucidate the operative mechanisms associated with quench cracking.

S/N	Specimen Orientation	Test Temp. (?F)	Axial Strain Rate to 0.02² (/s)	Disp. Rate (in./s)	Cooling Rate (?F/min.)
J866.D13	Tang.	2025	0.0006	0.01	125
J866.D01	Tang.	2000	0.0006	0.01	125
J866.D02	Tang.	1950	0.0006	0.01	125
J866.D03	Tang.	1900	0.0006	0.01	125
J866.D04	Tang.	1850	0.0006	0.01	125
J866.D05	Tang.	2050	0.0006	0.0002	125
J866.D10	Tang.	2050	0.0006	0.00012	125
J866.D06	Tang.	2000	0.0006	0.00012	125
J866.D07	Tang.	1950	0.0006	0.00012	125
J866.D08	Tang.	1900	0.0006	0.00012	125
J866.D09	Tang.	2050	0.0006	0.01	250
J866.D11	Tang.	2000	0.0006	0.01	250
J866.D12	Tang.	1950	0.0006	0.01	250

Table 7. GEAE supplied proprietary R104 on cooling tensile test data and specimens

1.5.2 Quench Crack Behavior Analysis

Fractographic analysis by OSU has enabled segregation of the specimens by fracture character. Two fracture regimes were observed. The first regime was one of apparent low ductility with a strongly intergranular character to the fracture surface. This observation was consistent with the macro measurements of low ductility. These specimens represented the lower test temperature regime. A second regime of apparent higher ductility was correlated with a ductile tearing fracture mode. This second regime was observed in the higher test temperature

regime. The nature of the fracture character correlated precisely with observed ductility measurements as shown in the following figure.
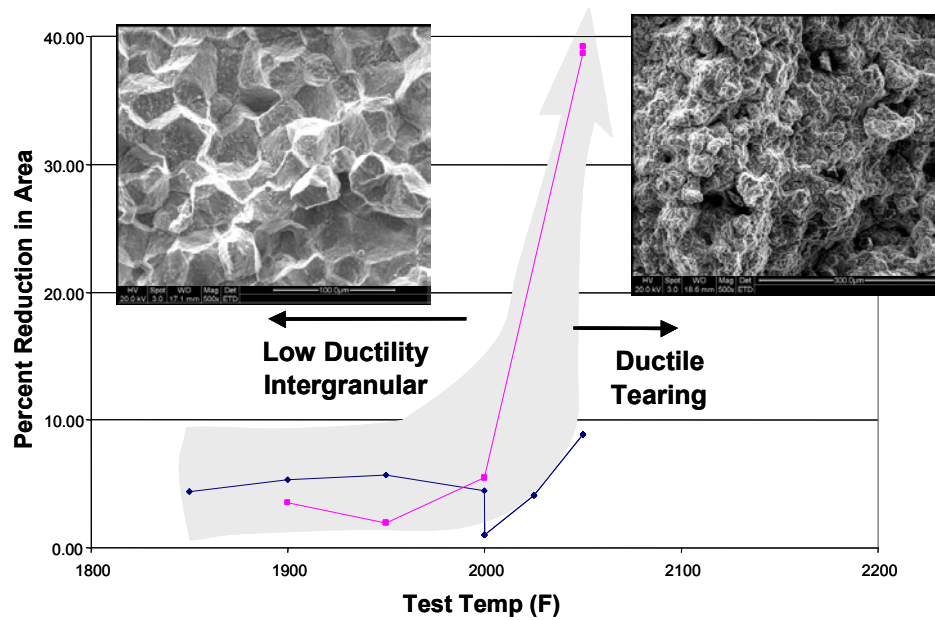
Figure 32 Regimes of high and low ductility for quenched R104 material and dominant fracture characteristics.

On cooling tensile test data test specimens for alloy R104 was also analyzed to determine values of strain hardening and strain-rate hardening exponents as a function of test temperature. The analysis indicates that large and important changes in mechanical behavior occurs in the vicinity of 2000 ºF consistent with the fractographic observations of the intergranular fracture regime.

$$\sigma = A\varepsilon^n\dot{\varepsilon}^m$$

Low Strain Rate R104-OCT Tensile Behavior
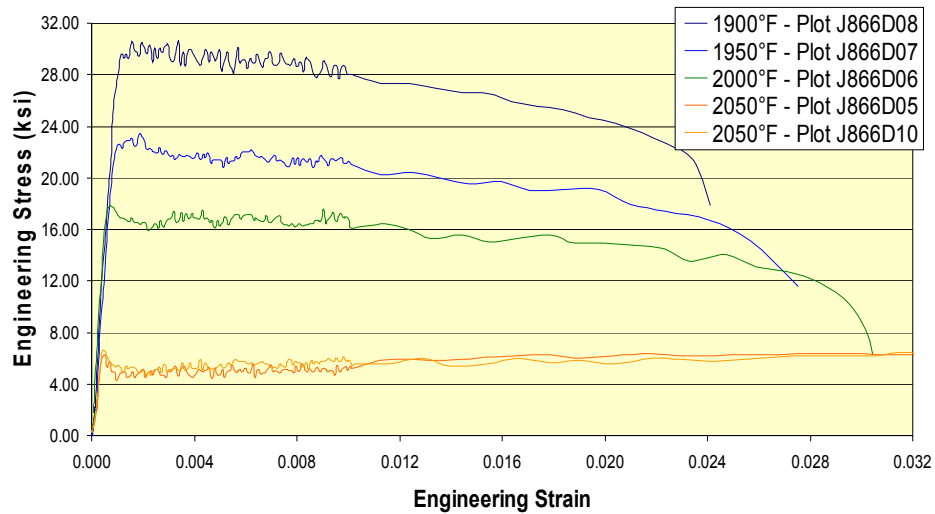
Figure 33 Constant strain rate on cooling tensile data for R104 used for determination of the strain-hardening exponent

Strain hardening exp (n) vs T:

$$n = \left(\frac{\partial \log \sigma}{\partial \log \varepsilon} \right)_{\dot{\varepsilon}}$$
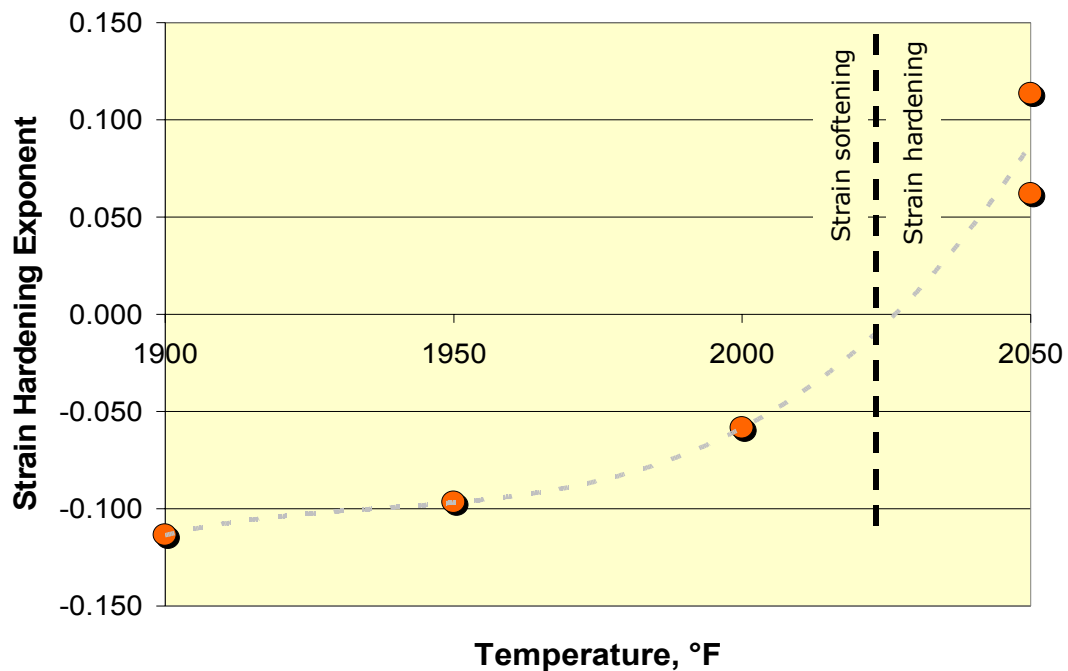
Figure 34. Strain hardening and strain-rate hardening exponents as a function of test temperature

Below this temperature, the ductility is < 5%, strain hardening is negative, and strain-rate hardening is relatively small. At 2050 ºF, ductility is relatively high with positive strain hardening and strain-rate hardening is nearly double that below 2000 ºF. Thus, the ductility transition at 2000 ºF correlates well with abrupt transitions in strain and strain-rate hardening. Initial efforts at setting up constitutive models have been completed at OSU and this information was used to frame the model requirements.

$$\sigma = A\varepsilon^{n}\dot{\varepsilon}^{m}$$

High Strain Rate R104-OCT Tensile Behavior
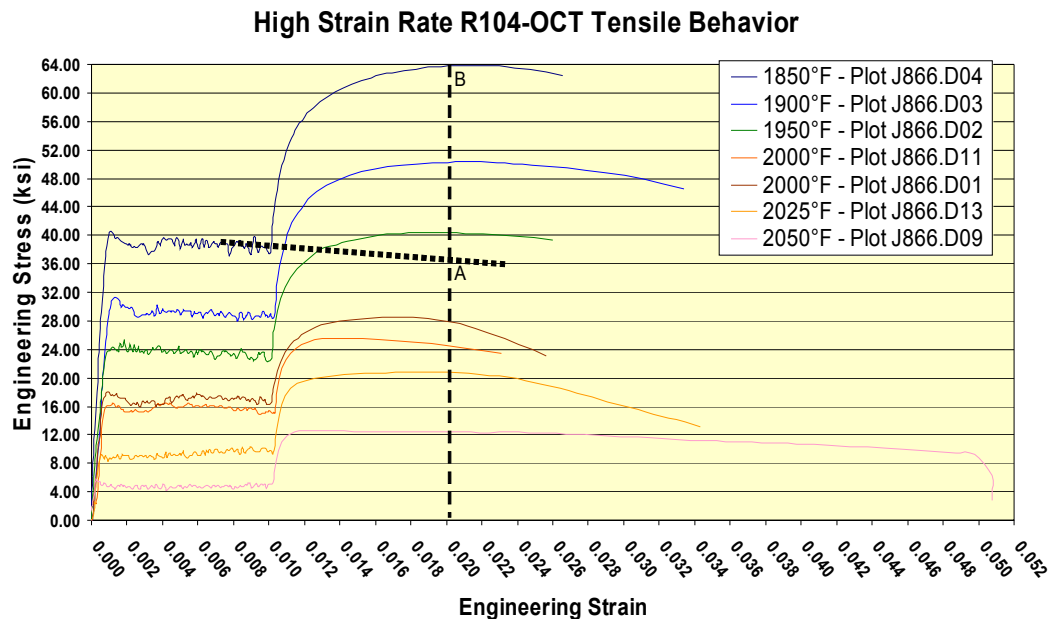
Figure 35. Variable strain rate on cooling tensile data for R104 used for determination of the strain rate sensitivity.

Strain rate sens (m) vs T:

$$m = \left(\frac{\partial \log \sigma}{\partial \log \dot{\varepsilon}} \right)_{\varepsilon}$$
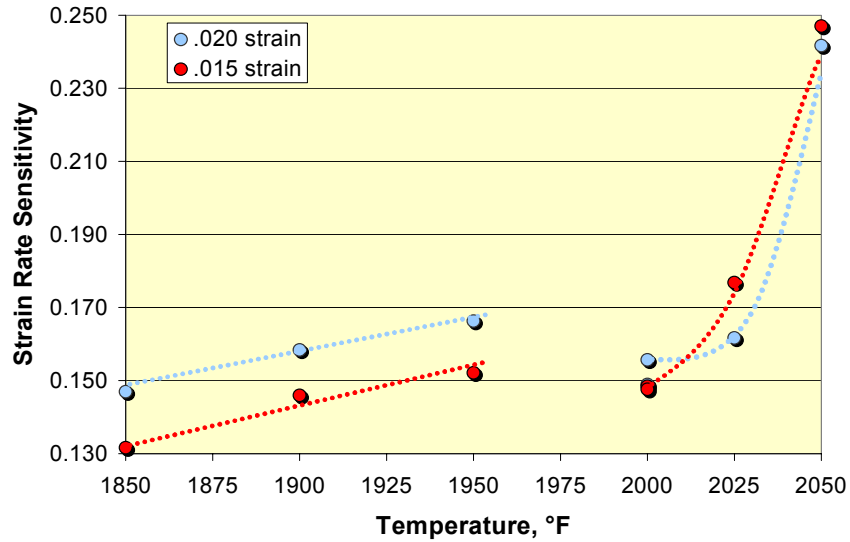
Figure 36. Strain rate sensitivity as a function of temperature.
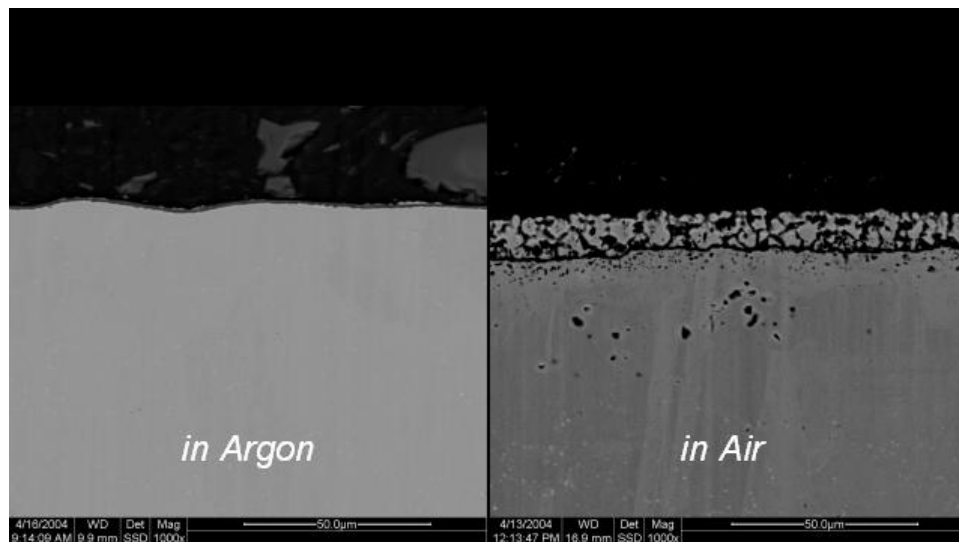
Figure 37. Evaluation of the effect of different atmospheres has been performed to define if voiding and embrittlement occur primarily due to oxygen exposure during heat treatment.

Also microscopy results indicate significant changes in the vicinity of the fracture surfaces and sidewalls during elevated temperature testing in air. This information supplements our earlier observation that the failure mode transitions from intergranular fracture in the range 1900 to 2000 ºF to ductile tearing at 2050 ºF.

(a)   (b)   (c)
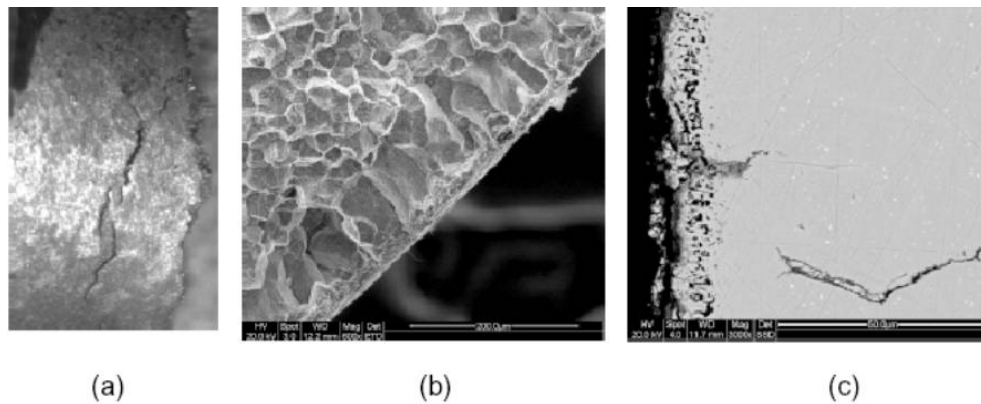
Figure 38. Integrated fractography and microscopy are utilized to determine origin locations and local microstructure.

Additional fractographic and metallographic studies are key areas for future work especially when augmented by additional on cooling tensile experiments.

SEM Image of crack in side wall of polished tensile specimen

OIM plot of side wall crack, with area grains assigned colors by orientation

30.00 µm = 60 steps   IQ 5.797...347.694, IPF [001]
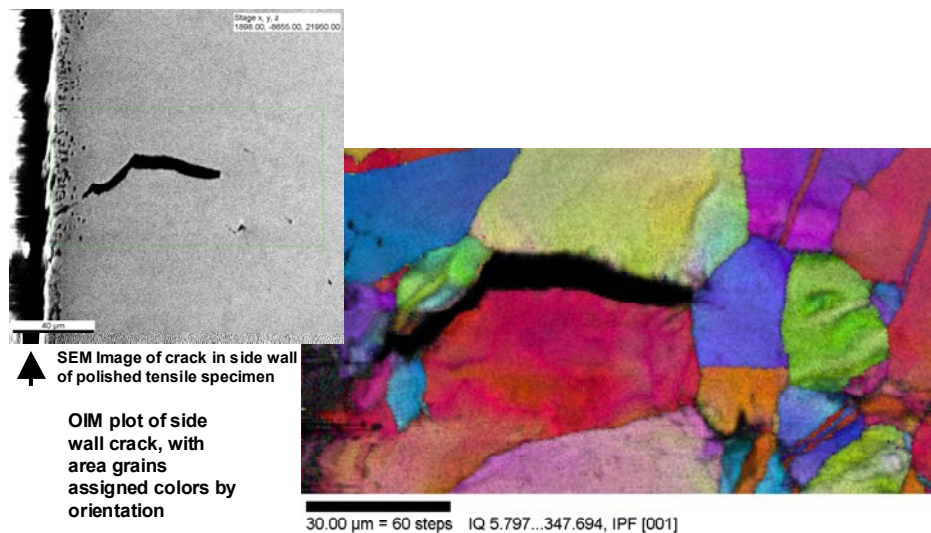
Figure 39. Orientation imaging work has initiated to determine if voiding and crack formation occurs preferentially on grain boundaries of certain misorientations.

Work on orientation imaging was just underway as of the writing of this report and will be discussed more fully by OSU in their final report to NASA.

1.5.3 Finite Element Model Development

During quenching strong thermal gradients get set up in the material that can lead to large hydrostatic pressure in the material. This can generate grain boundary yielding and the development of cracks. OSU's approach to the problem uses a yield function based on hydrostatic stress.

Since cracking at the grain boundaries is operative a three-dimensional interface model has been developed with a thin interface region between the two adjacent surrounding regions. The matrix materials are modeled using J2 plasticity while the interface region is defined using plasticity for porous materials represented by the Tvergaard-Gurson model, and is representative of the grain boundary. This model accommodates ductile failure by void initiation and growth. Due to symmetry one-eighth of the model has been taken for analysis and preliminary results are shown in the following figure.

Temperature variation in axisymmetric model of the turbine disc

Local

For initial void volume fraction

Macroscopic hydrostatic stress variation

Periodic boundary conditions applied

Interface representing grain boundary defined by Gurson model

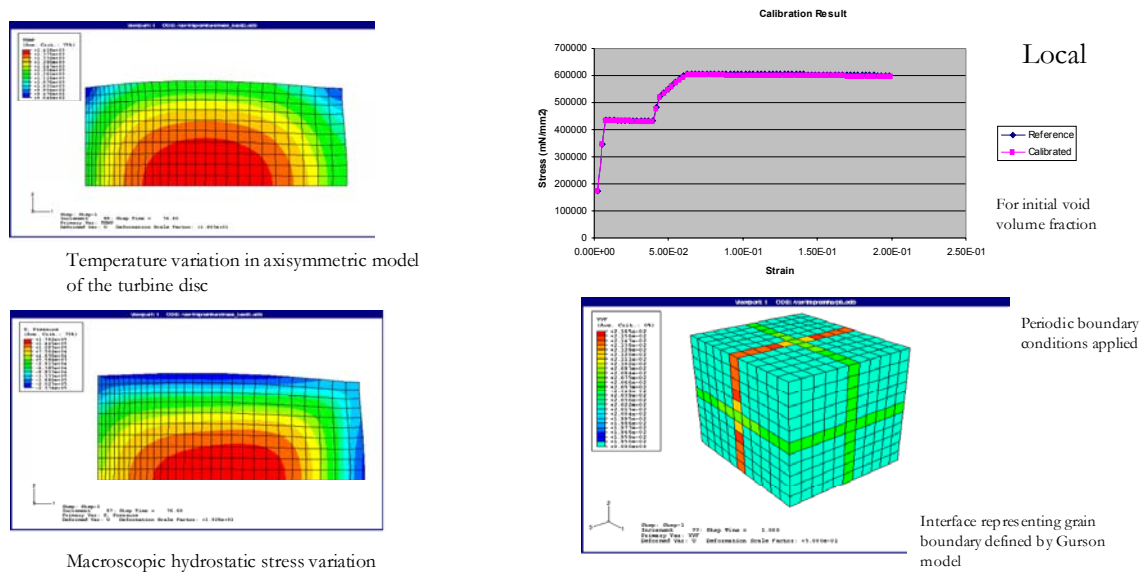Figure 40. Microstructural level finite element model framework developed for quench crack modeling.

Work on finite element will be discussed more fully by OSU in their final report to NASA.

1.6 Summary

A significant body of accomplishments has been achieved in the first year of the disk life meter activity:

Diffusion multiples

- Structural analysis techniques developed/refined that employ state-of-the-art capabilities at OSU for preparation of site-specific TEM samples (using the FIB) with rapid structure characterization (using EFTEM)

- EFTEM procedures well in-hand, FIB processes have been refined for superalloy samples. Approach enables securing samples from selected localized regions enabling detailed characterizations of local microstructural or deformation effects.

- Future work has been identified including analysis of actual diffusion multiples to define potential compositions with improved gamma prime stability/creep resistance, and integrate the analysis techniques into the creep, corrosion and quench crack tasks to better define local deformation mechanisms and regimes.

Creep Deformation

- Identification of the dominant deformation processes for relevant stress and temperature regime for R104.

- Observation of a new thermally-activated micro twinning deformation mode between 1200 and 1400 °F has been confirmed

- Facile by-pass of secondary g' precipitates at 1400 °F suggests there exists a fundamental upper bound temperature for useful creep resistance via gamma prime strengthening.

- A first generation, physically-based R104 creep model has been developed that accounts for novel micro twinning process and incorporates transitions in mechanisms. This work is key to initial definition of a disk life meter based on actual operating temperatures and times.

- Future work has been identified including interrupted creep testing to validate the micro-twining mechanism, evaluation of the stability of remote temperature measurement techniques, and extending the work to characterization of creep-fatigue interaction damage at a crack tip.

Corrosion studies

- A new hot temperature corrosion test has been established to accurately replicate engine turbine disk corrosion

- Work has identified the corrosion mechanism details and the effect corrodant on corrosion initiation

- Evaluation of time and temperature effects on the corrosion rate of reaction has been completed. This work is key to initial definition of a disk life meter based on actual operating temperatures and times.

- Corrosion mechanism understanding developed has allowed for understanding of potential protection schemes that will reduce the corrosion rate.

- Future work has been identified including 1) Expanding the corrosion model to include corrosion mechanism versus time of exposure and chemistry effects, 2) Further mechanism verification by cross-sectional analysis of corrosion morphology, 3) Expand the multiphase corrodant phase diagram understanding

Quench cracking

- Mechanical factors including strain hardening and strain rate sensitivity have been correlated with test temperature, observed ductility and fractography

- Fractography has identified a possible environmental effect for voiding as a component in the quench cracking.

- Finite element framework has been developed to model quench cracking at a microstructural level. The model is framed to incorporate the mechanical and fractographic findings.

- Future work has been identified including new testing, orientation image mapping, composition profiling and integrated finite element modeling. This work will be key to initial definition of a disk life meter based on actual operating temperatures and times.

REPORT DOCUMENTATION PAGE

Public reporting burden for this collection of information is estimated to average 1 hour per response, including the time for reviewing instructions, searching existing data sources, gathering and maintaining the data needed, and completing and reviewing the collection of information. Send comments regarding this burden estimate or any other aspect of this collection of information, including suggestions for reducing this burden, to Washington Headquarters Services, Directorate for Information Operations and Reports, 1215 Jefferson Davis Highway, Suite 1204, Arlington, VA 22202-4302, and to the Office of Management and Budget, Paperwork Reduction Project (0704-0188), Washington, DC 20503.

1. AGENCY USE ONLY (Leave blank)	2. REPORT DATE	3. REPORT TYPE AND DATES COVERED
	November 2005	Final Contractor Report

4. TITLE AND SUBTITLE

Disk Life Meter
Annual Report 2004

6. AUTHOR(S)

Dave Mourer, Brian Hazel, and Deb Whitis

5. FUNDING NUMBERS

WBS–22–714–92–50
NAS3–01135
Task order 23

7. PERFORMING ORGANIZATION NAME(S) AND ADDRESS(ES)

General Electric Aircraft Engines
One Neumann Way
Cincinnati, Ohio 45215–1915

8. PERFORMING ORGANIZATION REPORT NUMBER

E–15292

9. SPONSORING/MONITORING AGENCY NAME(S) AND ADDRESS(ES)

National Aeronautics and Space Administration
Washington, DC 20546–0001

10. SPONSORING/MONITORING AGENCY REPORT NUMBER

NASA CR—2005-213974

11. SUPPLEMENTARY NOTES

Project Manager, Clayton L. Meyers, Aeronautics Division, NASA Glenn Research Center, organization code PRV, 216–433–3882.

12a. DISTRIBUTION/AVAILABILITY STATEMENT

Unclassified - Unlimited
Subject Category: 07

Available electronically at http://gltrs.grc.nasa.gov

This publication is available from the NASA Center for AeroSpace Information, 301–621–0390.

12b. DISTRIBUTION CODE

13. ABSTRACT (Maximum 200 words)

The disk life meter specific objectives are to develop materials, models, and sensors to measure remaining life in turbine disk materials operated at sustained high temperatures of 1200 to 1500 °F for up to 20 000 hr. Initial physical models have been developed and future work can now expand the models and initiate sensor development and system integration towards a "disk life meter" based on remaining disk life using specific part operating conditions. Advanced analytical techniques were developed to characterize local chemistry effects on precipitation kinetics and morphological stability of gamma-prime during long-time exposure. This technique also has great promise in identifying local deformation mechanisms to calibrate physical model development. Advanced analytical techniques were also developed to characterize damage accumulation and failure modes associated with creep deformation, tensile rupture, and hot corrosion. R104 (General Electric Aircraft Engines, Cincinnati, Ohio) creep deformation modes were shown to be dependent on the stress/temperature regime and novel creep deformation modes were identified. Hot corrosion studies identified detailed aspects of the mechanism and point towards potential techniques to combat field corrosion. Quench crack studies have identified physical and mechanical behavior regimes associated with high and low ductility. Initial microstructural level FEM models have been established to further explore quench behavior.

14. SUBJECT TERMS

Propulsion systems (aircraft)

15. NUMBER OF PAGES

49

16. PRICE CODE

17. SECURITY CLASSIFICATION OF REPORT	18. SECURITY CLASSIFICATION OF THIS PAGE	19. SECURITY CLASSIFICATION OF ABSTRACT	20. LIMITATION OF ABSTRACT
Unclassified	Unclassified	Unclassified	